Article

Air Storage Impact on Surface Evolution of Stoichiometric and Li-Rich NMC811

Magdalena Winkowska-Struzik, Dominika A. Buchberger,* Witold Uhrynowski, Michał Struzik, and Andrzej Czerwinski

Read Online

ACCESS | Metrics & More | Article Recommendations | SI Supporting Information

ABSTRACT: In recent years, a type of layered oxide, $LiNi_xMn_yCo_zO_2$ (NMC) where $x+y+z = 1$, has become the preferred cathode material for electric vehicle (EV) batteries. Despite some disorder in the crystal structure due to Li^+/Ni^{2+} cation mixing, the composition offers a high specific capacity of up to 200 mAh g^{-1} at 4.3 V vs LiLi$^+$. The objective of this study is to comprehensively evaluate the structural and electrochemical changes in NMC811 after storage in ambient conditions. In this report, we study stoichiometric and Li-rich NMC811 in terms of their structural, morphological, and electrochemical differences. Following literature reports, a rigorous aqueous washing procedure was used alternatively to remove a possible lithium excess from the NMC surface. The findings of this study hold immense significance as they focus on the potential challenges that may arise due to the remaining lithium content or Li$^+$ extraction from the near-surface NMC811 materials. There is no consensus in the literature on whether excess lithium can harm the material's structural and electrochemical properties, reduce performance and safety concerns, or be beneficial regarding its protective properties, for Ni-rich NMC. Proper treatment of as-synthesized Ni-rich NMCs helps to develop procedures to address the residual lithium compounds issues, leading to enhanced performance and safety. Here with this report, we show another aspect not being considered in the literature before, regarding morphological NMC811 reshaping and a mechanism of LRC transition and growth due to aging. In addition, we linked the selected structural parameters to the electrochemical performance of various NMC811 materials. We discuss the well-known structural factors and their limitations and introduce a doublet resolution criterion that can help in predicting electrochemical performance.
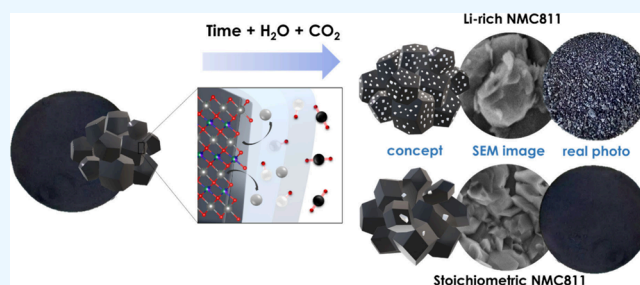
INTRODUCTION

Over the past decade, Ni-based layered oxides with the chemical formula $LiNi_xMn_yCo_zO_2$, where $x+y+z = 1$, became "a first choice" cathode material for EV batteries, surpassing cubic spinels ($LiMn_2O_4$) or olivines ($LiFePO_4$), owing to its high specific practical capacity vs LiLi$^+$ 185 mAh g^{-1} at 4.2 V[1] and reaching even 200 mAh g^{-1} at 4.3 V[2] for $LiNi_{0.8}Mn_{0.1}Co_{0.1}O_2$, shortly NMC811. An increase in the energy delivery from the NMC's materials family could be achieved in two ways: (1) through increasing Ni-content in the structure: NMC111 → NMC532 → NMC622 → NMC811,[3] or (2) shifting the upper cutoff voltage to higher values from 4.0 to 4.6 V vs LiLi$^+$. However, when there is higher Ni content in the NMC, the upper voltage limit should be set at a lower value, since above 4.3 V, Ni-rich NMC becomes structurally unstable and phase transition to rock-salt occurs due to high reactivity of Ni^{2+} at charged state.[4,5]

Despite its capacity advantage over other cathode materials, Ni-rich NMC suffers from structural disorders related to cation interexchange. This phenomenon is called *cation mixing*, where Li ions tend to partially occupy Ni ions lattice 3*b* sites, while Ni ions occupy Li ion 3*a* sites to minimize Coulomb energy and maintain the charge neutrality of the NMC crystals. Structural intermixing of cations is possible due to similar ionic radii of Li$^+$ (0.76 Å) and Ni^{2+} (0.69 Å) in octahedral coordination and is intensified in high-nickel NMC materials.[6] Once a certain concentration level is reached for the Ni/Li exchange, cation mixing leads to increased disorder in the crystal structure that blocks lithium diffusion pathways, which impedes electrochemical performance, cycle life, and capacity.[7,8] Ni-rich NMC can achieve reversible capacity around 200 mAh g^{-1} for NMC811; however, this value is regarded as an upper limit due to lattice oxygen release upon a high degree of delithiation and collapse of the bulk structure of NMC.[9−11] Another drawback of Ni-rich NMCs is the high reactivity of Ni

ions with an electrolyte, particularly in a charged state. This leads to electrolyte decomposition and gas evolution, followed by the decomposition of NMC particles, and the formation of cathode electrolyte interphase.[12]

Considering the supply chain of Li-ion battery manufacturing, one needs to take into account that the prolonged storage conditions of Ni-rich NMCs can lead to surface impurity formation.[13−19] And if one compares the open circuit voltage of $LiCoO_2$ and $LiNiO_2$, which are near 3.9 and 3.5 V vs Li|Li$^+$, respectively, it is clear that Li ions are more prone to deintercalation from the Ni-rich NMC interior than from Co-rich materials, to form lithium residual compounds (LRC).[20−22] Thus, Ni-rich NMC powder stored in ambient air can react first with atmospheric moisture and then with CO_2, leading to Li deintercalation and the formation of LiOH, $LiHCO_3$, and Li_2CO_3 on the powder surface, accompanied by the oxygen release.[23,24] These chemical transformations have been attributed to an H$^+$/Li$^+$ ion exchange and were confirmed by structural, spectroscopic, and electrochemical studies, and CO_2 titration with DFT calculations, as well.[14,17,25] However, LRC is also formed on the surface during the synthesis at high temperatures, since typically 1−25 mol % extra Li is added to balance its loss during thermal treatment[26−29] and to provide excellent structural ordering,[30,31] and good electrochemical performance.[29,32] When a stoichiometric amount of lithium is used for the synthesis of NMC, then only a negligible level of lithium residual compounds remains on NMC.[33] In both cases, LRC exist on the grains' surface and are responsible for parasitic reactions with an electrolyte.[16,34−36]

Adding significant surplus lithium to the synthesis not only minimizes the negative effect of a cation mixing but also promotes the formation of micron-sized single-crystalline NMC material instead of secondary particle morphology.[37−41] Those secondary round-shaped particles are composed of primary grains. An electrolyte can penetrate the particle bulk through the grain boundaries. In contrast, random crystallographic orientation of the primary grains leads to significant stresses as the crystallite volume changes upon intercalation and deintercalation of lithium ions, promoting cracking along grain boundaries, intense solid-electrolyte interphase formation, and breaking Li diffusion pathways, lowering NMC electrochemical performance.[29,42−49] The single-crystalline approach seems more beneficial since the NMC-based positive electrode can pass thousands of cycles with minimal capacity loss, minimal impedance growth, and no microcracking.[50,51] Improved volumetric energy density and rate capability are also reported.[52−54] On the other hand, the presence of LRC causes slurry preparation difficult and affects further cell performance.[34,55−59] Too high LRC content (>150 μmol per gram of NMC) can cause slurry gelation or flocculation,[60,61] as polyvinylidene difluoride (PVDF) exposure to strong alkaline conditions (pH ≥ 11) leads to dehydrofluorination reaction, caused by the removal of hydrogen and fluorine forming hydrofluoric acid (HF).[62,63] The dehydrofluorination degradations visually appear as a color change from white toward yellow to brown, concurrent with the C=C double bond formation, and manifests as the gelation of a PVDF solution due to the formation of cross-links between adjacent PVDF chains.[62,63] Dissolution of PVDF during slurry preparation occurs in N-methyl-pyrrolidone (NMP), which is stable under neutral conditions, but when exposed to an alkaline environment, its lactam ring can be easily hydrolyzed to produce 4-(methylamino)butanoate; the reaction can also be induced by

elevated temperatures.[64−66] Nonetheless, studies show that a slight amount of residual lithium (about 20 μmol per gram of NMC) can be beneficial for cell performance.[33,60,67] Therefore, there is a need to find a balance between a single-crystalline morphology promoted through excess Li and slurry stability during the electrode preparation.

Additionally, preventing the uncontrolled formation of LRC on the surface of Ni-rich NMC materials is crucial due to the challenges with PVDF and NMP decompositions[68] resulting in active material dissolution due to reaction with HF.[69] To minimize the number of side reactions, it can be beneficial to establish a physical barrier that prevents air moisture and CO_2 from coming into contact with NMC particles. This approach can slow down the rate of unwanted reactions, thereby improving the overall performance and durability of the system. To date, several approaches have been studied to create a protective layer on the NMC surface in the coating process with oxides or phosphates,[70−77] storage in an inert atmosphere, or by a simple washing procedure.[33,78−85] In comparison with pristine samples, coated materials exhibit improved cycle and thermal stabilities, but the protective layer must be thick enough to avoid contact with the H_2O/CO_2 from the air or with electrolyte, and also as thin as possible to enable high Li$^+$ diffusion and to keep a reasonable electronic conductivity.[70−76]

However, there is another aspect that we should take into account, concerning the LRC presence in the electrode layer. Adding lithium carbonate to the ethylene carbonate (EC), diethylene caronate (DEC) or dimethyl carbonate (DMC) suppresses the formation of CH_3 radicals from organic solvent, and the total amount of hydrocarbon gases (like CH_4, C_2H_4, C_2H_6, etc.). At the same time, the main gaseous product (CO_2) comes from the decomposition of the electrode material.[86,87] There is no consensus in the literature on whether Li_2CO_3 decomposes chemically or electrochemically. On the one hand, the formation of lithium carbonate, even at trace levels, will harm the stability of the Li-ion system due to the oxidation of Li_2CO_3 at a potential of ca. 3.8 V,[88] while lithium carbonate decomposition is activated by protic species formed above 4.6 V vs Li|Li$^+$, trace water, or HF impurities.[36] On the other hand, Li_2CO_3 was employed as a surface stabilizing agent in all-solid-state batteries to prevent layered cathode material degradation upon ambient storage.[89,90]

This study examined the morphological surface reconstruction of stoichiometric and Li-rich NMC811 and changes in their structural parameters among different synthesis routes to elucidate the mechanism behind the improved electrochemical performance of long-time-aged NMC powders. In addition to X-ray diffraction (XRD), we applied scanning electron microscopy (SEM) analysis and Raman spectroscopy mapping to identify the LRC and their postsynthetic and aging-related distribution. This is the first study implemented for liquid electrolyte Li-ion batteries concerning the influence of LRC on the morphology and electrochemical performance. We selected four structural parameters that can be used to correlate the electrochemical performance with the crystal quality of NMC811.

■ MATERIALS AND METHODS

Synthesis of NMC811. The synthesis procedure for NMC811 consists of two stages: hydroxide precursor synthesis via coprecipitation followed by thermal treatment with lithium source.[26,91,92] Briefly, a 2.0 M transition metal sulfate

($TMSO_4$) solution was prepared by dissolving $NiSO_4 \cdot 6H_2O$, $CoSO_4 \cdot 7H_2O$, and $MnSO_4 \cdot H_2O$ (Sigma-Aldrich) in deionized (DI) water with an 80:10:10 ratio, respectively. Simultaneously, a 10 M NaOH (Sigma-Aldrich) solution and 5 M NH_4OH (Chempur, Poland) were used as precipitation and complexing agents, respectively. All precursors were used as purchased. The $TMSO_4$, NaOH, and ammonia−water solutions were dripped into a three-port flask separately, under an argon atmosphere, a stirring speed of 500 rpm, reaction time and maturing of 20h, reaction temperature set to 65 °C, and pH in the range of 10.5−11. The resulting precipitates were then centrifuged, washed with deionized water at least three times, and dried overnight in a vacuum oven at 65 °C. Finally, the precursor powder was obtained.

As prepared transition metal (TM) hydroxide was mixed with $LiOH \cdot H_2O$ (Sigma-Aldrich) in the molar ratio of Li:TM = 1.05:1 (stoichiometric) and 1.2:1 (Li-rich),[31] using an agate mortar and pestle, and then placed in a muffle furnace in alumina crucibles for thermal treatment. The synthesis proceeded as follows: (1) heating to 450 °C at a rate of 5 °C·min^{-1}, (2) keeping the isothermal temperature for 2 h to decompose hydroxides, (3) heating to 780 °C at a rate of 5 °C· min^{-1}, (4) keeping at 780 °C for 12 h for oxide formation, and (5) cooling. As a result, two NMC811 powder samples were collected, named ST-NMC811 for the stoichiometric sample with Li:TM = 1.05:1, and LR-NMC811 for the Li-rich sample with Li:TM = 1.2:1 (Supporting Information: Scheme S1). Both samples were divided into two equal parts, 1.5 g each, and placed in glass flasks with 15 mL of DI water, sealed, and put in an ultrasonic bath for 30 min for washing, followed by solid− liquid separation and drying overnight in a vacuum oven at 120 °C. Washed samples were named as follows: ST-NMC811-W, and LR-NMC811-W, where W stands for "washed". Aging studies were carried out in an open glass container for at least nine months in an ambient atmosphere (humidity, temperature, and CO_2 were not controlled). After aging, samples were labeled: ST-NMC811-A, ST-NMC811-WA, LR-NMC811-A, LR-NMC811-WA, where W = washed, and A = aged.

Prepared samples were subjected to various characterization techniques including scanning electron microscopy, X-ray diffraction, Raman spectroscopy, electrochemical studies, and inductively coupled plasma-optical emission spectrometry (ICP-OES).

SEM-EDS Analysis. The morphology and surface structure of the sample were examined using a scanning electron microscope FE-SEM, Merlin Carl Zeiss equipped with backscattered electron (BSE), secondary electron (SE) detectors, and Bruker energy dispersive spectrometer (EDS). The sample was mounted on a table by using conductive adhesive carbon tape. SEM images were acquired at an accelerating voltage of 3 kV and a working distance of 2.4−3 mm to investigate the microstructural features and surface characteristics; for EDS measurement, the voltage was set to 15 kV.

XRD Analysis. The crystal structure and phase composition of the samples were analyzed using powder X-ray diffraction (XRD) on a Panalytical Empyrean diffractometer fitted with a PIXcell-3D detector with Ni-filter for Cu K_α radiation ($K_{\alpha 1}$= 1.54060 Å, $K_{\alpha 2}$ = 1.54443 Å) in the 2θ range of 5° to 115° in steps of 0.02° in flat plate Bragg−Brentano geometry with an effective count time of 250 counts per step. Obtained data were analyzed using HighScore 4.0, Match!, and FullProf

software to identify phases present in the sample and to calculate structural parameters using Rietveld refinement.

Raman Spectroscopy. Raman spectroscopy was employed to investigate the vibrational modes and molecular structure of the sample. Raman spectra were recorded using a Renishaw inVia Raman spectrometer equipped with a He:Ne laser excitation source (λ = 633 nm), grating 1800 l/mm. To provide more statistical character of the recorded data, 625 single spectra were recorded from a 25 μm × 25 μm area to create a map. The acquisition time for each spectrum was 15 s, and WiRE 5.5 and OriginPro software were used for data analysis and peak assignment.

Electrochemical Studies. Electrochemical measurements were conducted to examine the electrochemical behavior and performance of the sample. Electrodes were prepared using a mixture of 80% (w/w) of the NMC active material with 10% (w/w) active carbon Vulcan XC72R (Cabot, Bristol, UK) as a conductive agent and 5 wt % solution of poly(vinylidene fluoride) (PVDF, Alfa Aesar, St. Louis, MA, USA) in N-methyl-2-pyrrolidone (NMP, anhydrous, 99.5%, Sigma-Aldrich, Burghausen, Germany) as a plasticizer. NMC and carbon components were thoroughly mixed using a mortar and pestle and placed in a glass vial with 5% PVdF in NMP preblend to obtain a homogeneous slurry, which was cast on aluminum foil using a doctor blade coater with a thickness of 200 μm. The coated foil was preheated at 55 °C in the air to evaporate NMP and then was dried at 120 °C for 12 h in a vacuum oven. Electrode discs of 9 mm diameter were punched from the foil, pressed at 6 tons/0.6361 cm^2, and dried at 120 °C for 24 h in a vacuum to remove the residual NMP and traces of water. The electrodes were then transferred to an argon-filled glovebox (MBraun LABstar, Garching, Germany) for cell manufacturing. A three-electrode Swagelok cell configuration was employed with metallic lithium (Sigma-Aldrich) as both the reference and counter electrodes. The electrolyte used was 1 M $LiPF_6$ in 1:1 (vol:vol) ethylene carbonate: dimethyl carbonate mixture, battery grade EC: DMC 50:50 (v/v, Sigma-Aldrich, St. Louis, MA, USA). Celgard 2325 (USA) foil with a diameter of 12 mm was used as a separator, previously soaked in an electrolyte for 48 h.

All of the electrochemical experiments were performed at room temperature using a multichannel potentiostat−galvanostat Biologic system (Biologic Science Instrument, USA) or Atlas 1361 (Sollich battery tester, Poland). Constant current measurements we carried out in the range of 2.9–4.3 V vs Li| Li$^+$. Open circuit potential (OCV) was recorded for 24 h, then 10 cycles at 0.1C followed by high-rate tests at 0.2, 0.5, and 1C for 5 consecutive cycles at each rate and then, again, 0.1C for 5 to 8 cycles. The C-rates mentioned in the text were calculated by considering 1C as a theoretical capacity of 275 mA g^{-1}. Data were collected and analyzed using Biologic and OriginPro software. At least 3 cells were made for each sample and were measured under the same experimental conditions to ensure the reliability of the results. Mean values and standard deviation were calculated.

ICP-OES Analysis. To determine the elemental composition of the sample, inductively coupled plasma optical emission spectrometry (ICP-OES) was employed. Before analysis, solid samples were dissolved in water or mineralized using diluted sulfuric acid, where necessary, supplemented with hydrogen peroxide, and heated. Appropriate dilutions of the obtained liquid samples were made to fit into the concentration ranges for the analyzed elements. The resulting, diluted solutions were
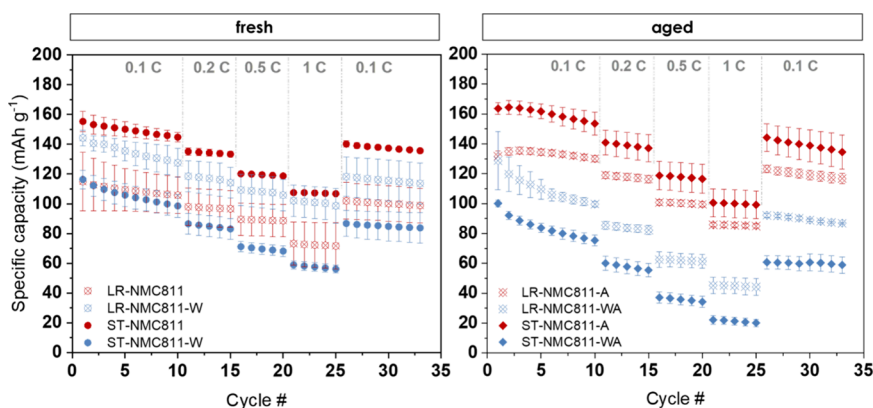
Figure 1. Electrochemical C-rate test results for fresh and aged NMC 811 samples (LR − stands for Li-rich, ST − stoichiometric, A − aged, W − washed, WA − washed and aged). Tests were carried out at room temperature for 10 cycles at 0.1C, 5 at 0.2C, 5 at 0.5C, 5 at 1C, and 10 at 0.1C.

analyzed using an Optima 5300 DV ICP-OES instrument (PerkinElmer, USA), and the concentrations of various elements were determined by comparing the sample signals with standard calibration curves.

Ex Situ XRD Measurements. Swagelok cells after C-rate tests were transferred to an Ar-filled glovebox (MBraun LABstar, Garching, Germany) for disassembling. The electrode was disassembled from the Swagelok, washed several times with dimethyl carbonate (Sigma-Aldrich, St. Louis, MA, USA) to remove electrolyte traces, and left for drying. Then electrodes were measured using the same setup and conditions as those for powder samples.

RESULTS

During the research on NMC811, we came across issues in the preparation of electrodes for freshly synthesized Li-rich NMC811 material. We noticed that the slurry suddenly thinned, which was opposite to the literature reports about gelation and flocculation.[60,61] To investigate this problem, we conducted experiments on controlled sample sets, including NMCs in stoichiometric and Li-rich compositions. We kept half of each sample as received from calcination to maintain LRC on the surface, and the other half was washed in water immediately after the synthesis to remove any potential lithium excess. Then, a portion of the samples were examined directly, and a part of them were aged for 9 months, to determine the effect of air storage on stoichiometric and Li-rich NMC811 (see Scheme S1 in Supporting Information (SI), page S-3). Through these experiments, we aimed to better understand the challenges associated with the preparation of NMC811 by Li-excess and washing as well as their ambient condition storage.

As discussed in the introduction, synthesis conditions and prolonged ambient storage promote LRC formation on the grains of Ni-rich NMC leading to PVDF degradation with HF release and TM etching and thus difficulties with slurry preparation. Polymer color change from white through yellow to brown is regarded as a fair indicator of PVDF degradation; however, in the presence of carbon black and dark gray NMC powder, it could be unnoticed. In our experiments on Li-rich NMCs, we observed a prominent slurry viscosity drop during the electrode preparation (SI, Figure S1a, page S-4), while other electrode layers based on stoichiometric and washed powders were prepared without such difficulties.[18,60] This wayward direction of sample preparation led to an investigation to understand and explain this effect. We have

checked the impact of three lithium compounds (LiOH anhydrous, LiOH monohydrate, and Li_2CO_3) on both solution of PVDF in NMP and NMP solvent alone (Figure S1b,c, respectively, page S-4) to have clear evidence of which compound has the strongest ability to decompose the polymer or the organic solvent. This experiment revealed that PVDF easily degrades in an alkaline environment; however, lithium carbonate also affects the polymer, but the effect is weaker. In the case of organic solvent, neither anhydrous nor monohydrate LiOH dissolves in NMP, while Li_2CO_3 makes it cloudy and slightly yellowish. Our observations were consistent with the literature reports.[60−62] After the LR-NMC811, the white lithium-based residue was visible without visual aids (Figure S2, page S-4).

Prior to further analysis, we started by evaluating the electrochemical performance of obtained NMC811 powders regarding the benefits or drawbacks of lithium addition, LRC removal, and aging. Based on electrochemical C-rate tests, shown in Figure 1, we have observed that the addition of extra lithium to the synthesis (Li-rich NMC811) or washing of stoichiometric powder has a similar impact on the electrochemical performance of *fresh* electrode powders. In contrast, washing of Li-rich NMC811 improves its specific capacity by about ca. 10−20 mAh g⁻¹. Stoichiometric fresh NMC811 (ST-NMC811) reaches 157 mAh g⁻¹ at the initial cycle and maintains around 140 mAh g⁻¹ after C-rate tests with a small standard deviation. Aged powders perform differently: ST-NMC811-A slightly improved its specific capacity at the first 0.1C cycles but after all performed similarly to its fresh analogue although with a greater degree of fluctuation. Stoichiometric washed material (ST-NMC811-WA) works even worse than its fresh counterpart (ST-NMC811-W) and reaches about 20 mAh g⁻¹ at 1C, only. Considering the aging effect on Li-rich NMC811, both washed and unwashed (LR-NMC811-WA and LR-NMC811-A, respectively), the materials significantly changed their electrochemical performance. Washed and aged Li-rich NMC811 material (LR-NMC811-WA) loses its capacity and reaches only ca. 100 mAh g⁻¹ after the C-rate tests, while aged Li-rich NMC811 (LR-NMC811-A) powder outperforms its fresh analogue by about 15 mAh g⁻¹, with a minor standard deviation in each cycle and greatly improved stability.

To shed more light and understand the material differences, we conduct morphology observations and analysis of fresh and aged samples both unwashed and washed. SEM images of all analyzed materials are presented in Figure 2. Li-rich unwashed
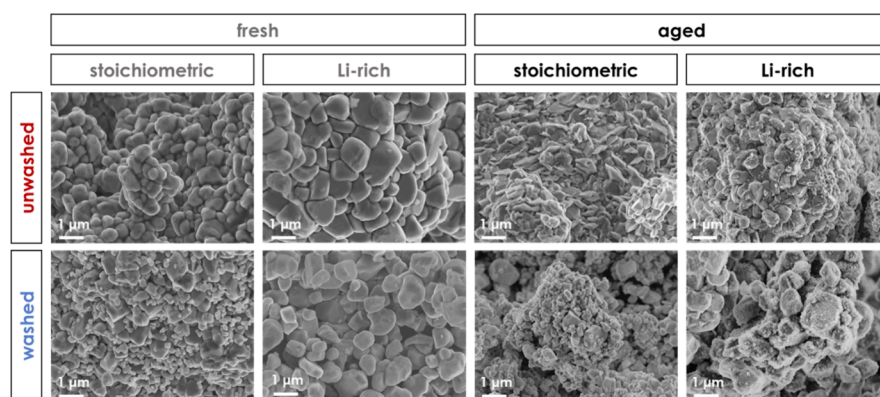
Figure 2. SEM images of all of the prepared NMC811 samples. A morphology change is visible upon aging of the unwashed stoichiometric samples with altered shape of observed particles. For Li-rich NMC811 aged samples surface becomes covered with LRC particles (LR-NMC811-A and LR-NMC811-WA). For stoichiometric washed samples (ST-NMC811-W and ST-NMC811-WA), no significant changes in surface morphology are observed after aging. The scale bar for all images is 1 μm.
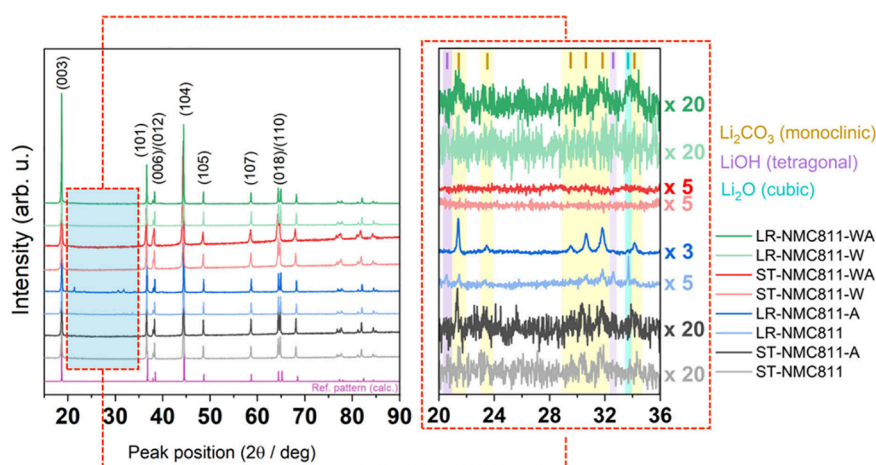

Figure 3. XRD patterns for all NMC811 samples with α-NaFeO$_2$-type layered structure of $R\overline{3}m$ space group symmetry (ICDD card no. 96-152-0790) with indexed reflexes,[30,98,99] and zoom of 2θ 20−36° angle range of LRC with identified phases of Li$_2$CO$_3$ (blue-yellow), Li$_2$O (turquoise), and LiOH (purple) with ICDD cards no. 96-900-8284, 96-151-4093, and 96-10-0302, respectively;[100] the signal at the zoom image was multiplied to magnify reflexes.

sample (LR-NMC811) is composed of agglomerates with slightly bigger particles than the stoichiometric sample (ST-NMC811) due to the influence of additional LiOH amount during annealing. It is known that the addition of significant alkali salt excess results in higher crystal growth since it acts like a flux to promote single-crystalline particle morphology, and 20% of lithium excess in our Li-rich sample could fulfill this requirement.[40,93−95] Additionally, the surfaces of the LR-NMC811 sample particles were unevenly covered with small flat precipitates, suggesting LRC residues (further confirmed by Raman spectroscopy). Removal of LRC from the particle surface was done by an ultrasound-assisted water-washing procedure performed on both Li-rich NMC (LR-NMC811) and stoichiometric NMC (ST-NMC811) samples to examine the efficiency and effect of such an approach. Considering only morphological aspects, agglomerates of Li-rich powder were composed of grains with a quite narrower particle size distribution from 300 nm to 1 μm. During rinsing particles in Li-rich agglomerates easily fragmented along weaker grain boundaries due to LRC existing on their surfaces and thus higher water reactivity (Li$_2$O) and solubility (LiOH) and revealing similar size distribution. In contrast, a wider particle size distribution from ca. 60 nm to 1 μm was observed for

powder with a stoichiometric amount of lithium only. After washing, the inside morphology of the unwashed agglomerate was uncovered: bigger particles composed of smaller grains were prone to fragmentation, and the smallest primary grains were detached first. Moreover, the XRD analysis revealed that the average crystallite size is smaller than the particles shown in SEM images of fresh powders, indicating their polycrystalline nature, as discussed further.

The change in morphology was observed for all samples after aging except stoichiometric washed powder (ST-NMC811-W and ST-NMC811-WA) for which no surface alteration after aging was observed, and nearly the same morphology as for the initial powder was obtained. On the other hand, the initially smooth egg-shaped particles of the stoichiometric unwashed sample (ST-NMC811-A) surprisingly changed into sharp-cornered ones. This effect is observed only for stoichiometric samples, in which particles are similar to inclined prisms. This phenomenon is only an outer surface transition of the agglomerate since in Figure 2, one can observe an intact interior, which was uncovered (partial mechanical removal) during sample preparation for SEM examination of sample ST-NMC811-A proofing the ambient storage effect on the sample surface only. For comparison purposes, we have
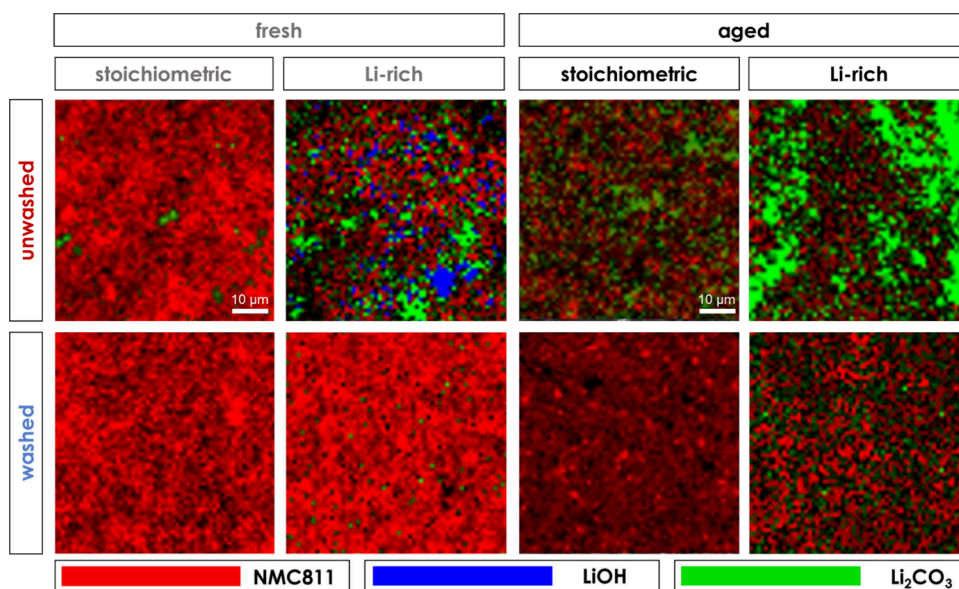
Figure 4. Raman spatial maps of fresh and aged NMC811 samples before and after the washing procedure: the red area is related to the intensity of NMC811 at A_{1g} mode, the blue area—to LiOH at 328 cm^{-1}, and the green area to Li_2CO_3 at 1088 cm^{-1} mode.

recorded SEM images for other batches of ST-NMC811, which were stored in ambient air as well as inside the glovebox, showing surface transformation occurred only due to ambient storage conditions (see Figure S3a-d, page S-5).

Initially, the LR-NMC811 sample (Figure 2) contained LRC on its surface, which looked like specks of dust. After storage, it changed into husks covering the whole powder confirming the postsynthetic growth of the additional phase on the Li-rich NMC811 surface, which was visible to the naked eye as a white precipitate (Figure S2, page S-4). Although, after washing, the LR-NMC811-W sample looked clean, its aging uncovered the hidden nature of the LRC. The surface of the washed and aged counterpart of Li-rich NMC811 powder, LR-NMC811-WA was uniformly sprinkled with a thin layer of ash-like powder of about 15 nm or smaller. Although SEM investigation revealed morphology changes upon washing and aging of Li-rich and stoichiometric materials' surfaces, it has not yet addressed the change of the slurry viscosity of LR-NMC811 powder; therefore, we looked into the crystal structure. Figure 3 and Figure S4 show the XRD patterns of the investigated materials. All XRD patterns consist of reflections typical for NMC811 in $R\bar{3}m$ space group; however, when assessing zoomed-in areas of the 2θ region between 20 and 36°, additional reflexes can be easily observed and further identified as LiOH, Li_2O, and Li_2CO_3 (Figure 3 zoom).[34] Lithium oxide (Li_2O) on the surface of active materials is a postcalcination residue derived from the extra amount of lithium added to compensate for its evaporation and minimize the cation mixing during the calcination process.[96] Li_2O can readily combine first with water molecules from air moisture at room temperature, forming LiOH, and further with carbon dioxide, forming Li_2CO_3.[97] Since those reactions proceed simultaneously, both byproducts are detected for the as-received Li-rich sample (LR-NMC811). Therefore, detected LRC, mainly LiOH, were responsible for the slurry thinning by PVDF defluorination and a loss of its plasticizing properties.[62,63]

XRD patterns of powders aged in ambient conditions reveal a greater phase contribution of LRC than for as-prepared samples (Figure 3 zoom). That could be explained by (1) the

presence of thin lithium hydroxide residue remained after washing, and over time transformed into a Li_2CO_3 which agglomerated into larger particles; (2) additionally, lithium ions are prone to diffuse to the grain surface due to the Li deficient region formed after washing and over time reacts with moisture and grow thicker LRC deposits.[101] XRD patterns revealed for Li-rich samples aged for 9 months under ambient conditions that mostly Li_2CO_3 can be detected with a trace amount of LiOH at the limit of detection (Figure 3 zoom). That suggests a complete transition from initially present Li_2O to LiOH and Li_2CO_3. Small amounts of LRC are also detected in ST-NMC811 and ST-NMC811-A samples, showing that Li_2CO_3 growth over time is not solely and directly responsible for the observed morphological change in stochiometric and aged NMC811.

Phase analysis based on XRD data did not reveal any phase transitions for the aged stoichiometric NMC811 sample (ST-NMC811); however, we cannot exclude that the change in morphology could be associated with a change from hexagonal to pseudocubic or monoclinic lattice systems owing similar XRD patterns,[102] as the consequence of lithium extraction from the near-surface grain. For stoichiometric washed powder (ST-NMC811-W) Rietveld refinements reveal the presence of a second, delithiated rock-salt phase (Figure S5, page S-7), formed during H$^+$/Li$^+$ exchange.[103] If we consider also an elemental composition analyzed by ICP-OES, there is clear evidence that washing of stoichiometric NMC811 causes lithium extraction from the sample (Table S1 and Table S2, page S-8). Lithium is removed not only from the particle surfaces due to a dissolution of Li compound residues but also from the NMC structure leaving about 96 molar% of lithium after washing (Table S3, page S-8). This could explain the lowest electrochemical performance and structural distortion of ST-NMC811-W in comparison to the other samples, especially for its unwashed counterpart, ST-NMC811. Detailed structural analysis (Table S4, page S-9) reveals that the Li-rich sample (LR-NMC811) shows a higher degree of structural ordering than stoichiometric (ST-NMC811); however, worsening of electrochemical performance can be associated with
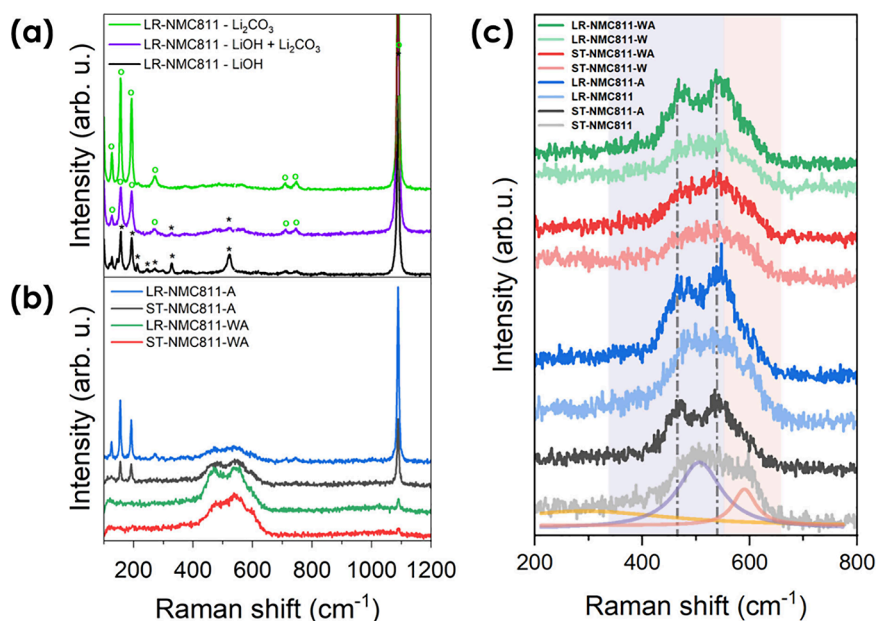
Figure 5. Raman spectra of investigated materials: (a) Raman spectra of the LR-NMC811 sample with marked modes related to impurities: LiOH and Li_2CO_3. (b) Raman spectra of all aged samples show a Li_2CO_3 impurity signal. (c) A comparison of NMC811 spectra of fresh and aged samples; light-violet zone — E_g mode, light-red zone — A_{1g} mode, dot-dash line — new Raman peaks from Li-deficient surface region at 470 and 545 cm^{-1}.

TM dissolution from the surface upon HF formation after OH^- radical attack on the PVDF chains. Rietveld refinement was used to calculate the ion occupations at each Wyckoff position, and since it is an indirect method, only the trend was analyzed. Although a higher cation mixing (Table S5, page S-10) was observed for the ST-NMC811 sample in comparison to the Li-rich analogue, it showed the highest discharge specific capacity among all synthesized samples (ca. 155 mAh g^{-1}).

Further, we move toward local structure analysis. Raman microspectroscopy gives a lateral resolution of about 1 μm, and thus applying the mapping mode we can gain a lot of qualitative and precise information about the sample composition (qualitative analysis). Figure 4 shows that a fresh unwashed Li-rich sample contains a tremendous amount of LiOH (blue area) and Li_2CO_3 (green area) on the surface of the NMC particles. Raman signal from the Li_2O, detected with XRD, overlaps with the NMC vibrational modes (band at 529 cm^{-1}), and thus, we could not separate those signals in the Raman maps.[104] Since the amount of LiOH is significant, it is obvious that those residues located on the surface of the fresh Li-rich sample did not fully transform into Li_2CO_3 upon ambient air exposure. As a consequence of the high concentration of LRC on the surface of powder grains, we observed the thinning of the PVDF binder during the slurry preparation. After aging, the unwashed Li-rich sample contains only Li_2CO_3 (green area) impurities, and therefore, the slurry preparation improved for that sample, as PVDF binder thinning did not occur. After washing the Li-rich material, only a minor scattered signal from Li_2CO_3 can be detected, showing that the full removal of LRC residues is challenging. During the aging process, the amount of Li_2CO_3 increases for the Li-rich sample, suggesting a partial reaction of Li-ion with air at the top surface of NMC811 material grains. In the case of the unwashed stoichiometric sample, only small localized fractions of Li_2CO_3 particles can be observed, whereas after aging, it revealed both localized fractions and a uniformly

spread small signal from Li_2CO_3 is visible, suggesting the reaction of surface Li ions with air. Only the fresh and washed stoichiometric NMC811 samples did not show LRC residues. However, for the ST-NMC811-W sample, the surface is modified due to the washing procedure, and we assume that this surface is likely Li-deficient, which significantly disturbs its electrochemical performance. After aging, the ST-NMC811-WA sample shows a minor but uniform coverage of a Li_2CO_3 signal (darkening of Raman map, as a consequence of green and red colors mixing during map preparation).

Figure 5a shows the Raman spectra of the compounds detected in the most contaminated sample, Li-rich unwashed NMC811. For the freshly made powder, we could observe both LiOH, Li_2CO_3, and their mixed signals. After they were aged, the LiOH crystals fully transformed into Li_2CO_3. Depending on the preparation procedure, aged samples showed stronger (LR-NMC811-A) or weaker (ST-NMC811-WA) signals. A small signal of the symmetric stretching vibration of the CO_3^{2-} groups located at 1088 cm^{-1} can be detected even for an aged washed stoichiometric sample (Figure 5b). It is also worth noting that this sample showed a disturbed Raman signal of the NMC structure. This is a representation of structural changes that happened after sample washing and partial structural reconstruction due to the sudden surface Li removal. Figure 5c shows Raman's response from as-received and aged samples. Typical Raman lines of NMC811 are fitted for the ST-NMC811 material. A_{1g} and E_g modes appear at 590 and 506 cm^{-1}, respectively, as expected for this NMC composition.[105] Only the ST-NMC811-W sample shows a disturbed A_{1g} to E_g ratio. After aging the samples, the growth of two new modes at ca. 470 and 545 cm^{-1} is observed (Figure 5c). These new bands remind the discharged NMC811 features indicating that over time Li ions react with air (H_2O and CO_2) diffusing from the near-surface region to the top and causing a Li-deficient region observed in Raman spectra.[105]
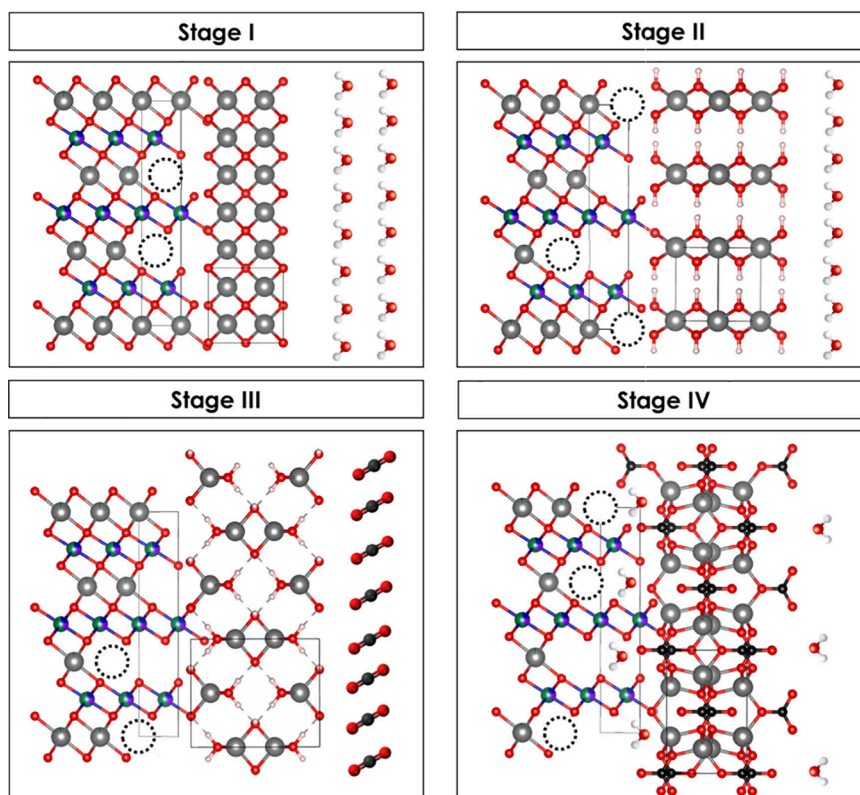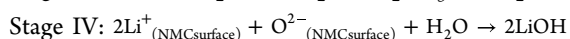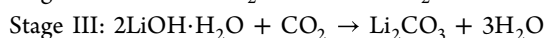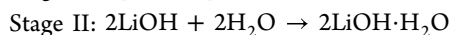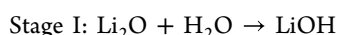
Figure 6. Schematics of LRC formation process: (Stage I) Li_2O postsynthetic residue quickly reacts with H_2O after cooling; (Stage II) LiOH created from Li_2O residue reacts with H_2O creating monohydrate; (Stage III) LiOH· H_2O further reacts with CO_2; (Stage IV) Water molecules released from Li_2CO_3 formation might further react with Li-ion out-diffusing to the top surface of NMC creating thicker LRC deposits and Li-deficient NMC grain shells.

From those experiments, we can conclude that there are four stages of creating LRC at the surface of NMC811 over time (Figure 6 and Figure S6, page S-11). The surface reactions can be described as follows:[106]

Stage I: $Li_2O + H_2O \rightarrow LiOH$

Stage II: $2LiOH + 2H_2O \rightarrow 2LiOH·H_2O$

Stage III: $2LiOH·H_2O + CO_2 \rightarrow Li_2CO_3 + 3H_2O$

Stage IV: $2Li^+_{(NMCsurface)} + O^{2-}_{(NMCsurface)} + H_2O \rightarrow 2LiOH$

During the first stage after cooling the postsynthetic Li_2O residue reacts with H_2O creating LiOH. It is known that the surface of Li_2O particles first converts into a LiOH layer followed by the bulk of the particle.[96] Williams et al. experimentally studied the transformation of LiOH into Li_2CO_3 at room temperature, and they concluded that it is a two-stage process. Since LiOH contains OH^- groups between (002) to (005) planes with a distance between Li–Li layers of 4.334 Å, water molecules of ~2.8 Å size can easily fit in and initiate the phase transition from $P4/nm$ tetragonal to $C2/m$ monoclinic structure. Consequently, in the second stage, LiOH created from the Li_2O residue further reacts with a moisture-formed LiOH monohydrate ($LiOH·H_2O$). In the third stage, $LiOH·H_2O$ reacts with CO_2 converting into Li_2CO_3 ($C2/c$ monoclinic structure). As seen in Figure S7 (page S-12, SI) the (220) plane of the $C2/m$ monoclinic structure can be exposed to CO_2 from multiple crystal facets: (201), (021), (20-1), and (11-1) planes located at various crystallographic directions giving more chances for the reaction to occur. This reaction produces three mol of water per mole of Li_2CO_3. Those released H_2O molecules might further react with Li ions

located near the NMC surface region, promoting the formation of the thicker LRC deposits and Li-deficient NMC grain shells.

After reaching stage IV the reaction can loop with stage II until there are no near-surface Li ions at the interphase with Li_2CO_3 ready to react with H_2O. Such mechanism might initiate additional surface changes such as TM surface reorganization (e.g., rock-salt formation) or the reaction of TM with air (e.g., $NiCO_3$), thus worsening the electrochemical performance of the material. As seen above, the effect of the ambient storage highly depends on the sample preparation, its final structure, and the amount and distribution of LRC at the NMC811 surface. Locally, grouped and larger LRC crystals seem to have a less severe impact on NMC performance than more uniformly distributed ones. This might be due to the overall smaller physical contact between NMC and formed Li_2CO_3 crystals because, due to their size, the most of lithium hydroxide particles transition to carbonate happens away from the NMC surface. In the worst-case scenario, the LiOH uniformly covers particle surfaces, transforms into Li_2CO_3, and releases moisture at the near NMC surface, thus initiating the further reaction with Li ions as in the case of Li-rich washed sample where LiOH homogeneously reprecipitates after washing.

We know from the literature that Li_2CO_3 is regarded as stable during electrochemical operation up to 4.6 V while in the presence of trace water or HF impurities may be chemically decomposed, forming LiF on the surface.[36] To examine the stability of the developed LRC upon C-rate test, electrodes with unwashed and aged NMC811 (LR-NMC811-A) active material were characterized using the *ex situ* XRD experiment,

before and after electrochemical measurements (Figure S8, page S-13). Received XRD patterns are typical for NMC811, with additional reflexes originating from amorphous carbon, aluminum foil, and Li_2CO_3. There are no reflexes from LiF or other phases from electrolyte degradation and cathode-electrolyte interphase formation. LRC present on the surface of the aged and unwashed LR-NMC811 (LR-NMC811-A) remains stable upon C-rate electrochemical testing to 4.3 V as expected.

DISCUSSION

Taking into account differences in the initial capacity and the shape of charge−discharge curves (Figure 1 and S9, page S-14, respectively), we see that the discussed differences in NMC811 structures and the presence of LRC play a major role in electrochemical performance. Unwashed and washed stoichiometric NMC811 differ in overpotential of the first cycle (ca. 100 mV higher for the washed sample) and irreversible capacity loss (52 vs 35 mAh g^{-1}, respectively), which is smaller for the aged powders in both cases of about 6−7 mAh g^{-1} (Figure S9, page S-14). This could be associated with a complete transition from lithium hydroxide to lithium carbonate. A similar situation was with Li-rich NMC811, where improved electrochemical performance occurred after the sample aging. Since LRC reflexes, observed in XRD data, are more prominent in Li-rich material, it was possible to identify initial residues as lithium hydroxide, oxide, and carbonate mixture (Figure 4). Knowing that a highly alkaline environment is responsible for HF release in defluorination and dehydrogenation of PVDF, a dissolution of transition metals in HF, and a change in surface chemistry of NMC particles of LR-NMC811 sample is a major drawback and source of electrochemical performance worsening.[107] Though we did not observe flocculation, gelation, or thinning of slurry during ST-NMC811 electrode preparation, we can assume that an analogous phenomenon of HF etching is possible but on a much smaller and more local scale.

Literature reports state that deionized water washing is a good strategy for LRC removal.[33,78,79,82−84] Indeed, a better electrochemical performance was observed for the washed Li-rich sample (LR-NMC811-W) in comparison to the unwashed analogue, while the stoichiometric NMC811 (ST-NMC811-W) material performed much worse and had the highest irreversible capacity loss during the first cycle (Figure S9, page S-14). This could be associated with a wider particle size distribution and lithium deficiency in the washed stoichiometric sample, which consequently partially forms the rock-salt phase near the surface upon delithiation in water solution (Figure 2, Figure S5, and Table S4). On the other hand, we can see that the aging of washed Li-rich NMC811 drastically changes its electrochemical performance, since in this case, the LRC had enough time to transition from LiOH into Li_2CO_3. Since the coverage of LRC is very uniform, the released moisture (stage IV) reacted with Li ions at the near surface of NMC, looping stage II to stage IV reactions creating the increased amount of LRC that are partially composed of lithium ions out-diffused from the NMC811 surface (Figure 2). This effect can also be observed as a change in charge and discharge profiles that does not remind the regular NMC behavior (Figure S9, page S-14).

Electrochemical performance is often linked to structural parameters in several manners. Typically, a calculation of the integrated intensity ratio of (003) and (104) reflexes from the XRD pattern is presented as a quality factor. To obtain NMC material with a good hexagonal ordering and reduced Li$^+$/Ni^{2+} cation mixing, it is often stated that this ratio should exceed the value of 1.2.[102,108,109] It should be mentioned that this value was calculated from experimental data of $LiNiO_2$ material and assumed for NMC analogs.[102,110] The second parameter, defined in literature as the $I(006 + 012)/I(101)$ ratio, is imprecisely claimed to have a value as small as possible.[109,111−113] The analysis of the doublet (018)-(110) centered at ca. 65° in 2θ range[30,98,109,111,113−115] is usually presented in two ways: by calculation of the doublet separation, and analysis of the doublet mutual peak position, and the $I(110)/I(018)$ ratio calculation.[116−121] In the first method, it is claimed that this doublet has to be "well separated", but no precise range is given. The second method with the $I(110)/I(018)$ ratio calculation is based on the fact that the [110] facet has an open layered interspace for lithium intercalation into the bulk material.[116−121] At the same time, there is no open space within the (018) plane due to the close-packed atomic structure. The orientation of grains can be deduced based on XRD patterns analyzing the (018)-(110) doublet. The intensity ratio of $I(110)/I(018)$ greater than 1 demonstrates (110)-oriented active planes and is regarded as a factor determining better electrochemical performance.[122]

Based on our experiment, we concluded that the integrated intensity ratio of (003)/(104) planes could be affected not only by cation mixing within the hexagonal structure but also by a partial phase transition from hexagonal to cubic, since (202) plane reflex of cubic phase overlaps with (104) reflex of hexagonal phase, leading to a virtual increase of (104) intensity, if only $R\overline{3}m$ phase is considered. On the other hand, the intensity ratio of $I(110)/I(018)$ could be insufficient for overlapping doublet reflexes (Figure S4, page S-6). Also, transition-metal−oxygen (TM-O) and lithium−oxygen (Li−O) slab thickness did not show any particular correlation with electrochemistry. Thus, the parameters mentioned above did not act as good quality factors for NMC811.

We have identified four major factors that correlate with the electrochemical performance of obtained NMC811 materials, namely, unit cell volume, intensity ratio $I_{(006+012)}/I_{(101)}$, crystal size, and newly described doublet resolution of (018)-(110) and (006)-(012) reflexes (Figure 7).

Based on our detailed analysis, we propose to introduce a definition of the doublet resolution (eq 1), adapting this term from gas chromatography analysis, as[123]

$$R_{(018-110)} = \frac{\Delta x_{(018-110)}}{\text{fwhm}_{(018)} + \text{fwhm}_{(110)}} \qquad (1)$$

where $R_{(018-110)}$ is a doublet resolution, $\Delta x_{(018-110)} = x_{(110)} - x_{(018)}$ (x-reflex position in 2θ range) is a doublet separation, fwhm is a full width at half maximum of selected reflex. Our intention was to replace doublet separation because this parameter is regarded as information about delithiation and seems to be less sensitive for deviation from perfect hexagonal ordering for $R\overline{3}m$ (Figure S10, page S-16). Additionally, doublet resolution not only contains information about the reflex position (similarly to the doublet separation), but also links the crystal size with the crystal quality. As seen in Figure 7, the crystal size is closely related to the doublet resolution and follows the same trend. We can see that both the crystal size and the doublet resolution have to be of the certain range to obtain a satisfactory electrochemical performance. For
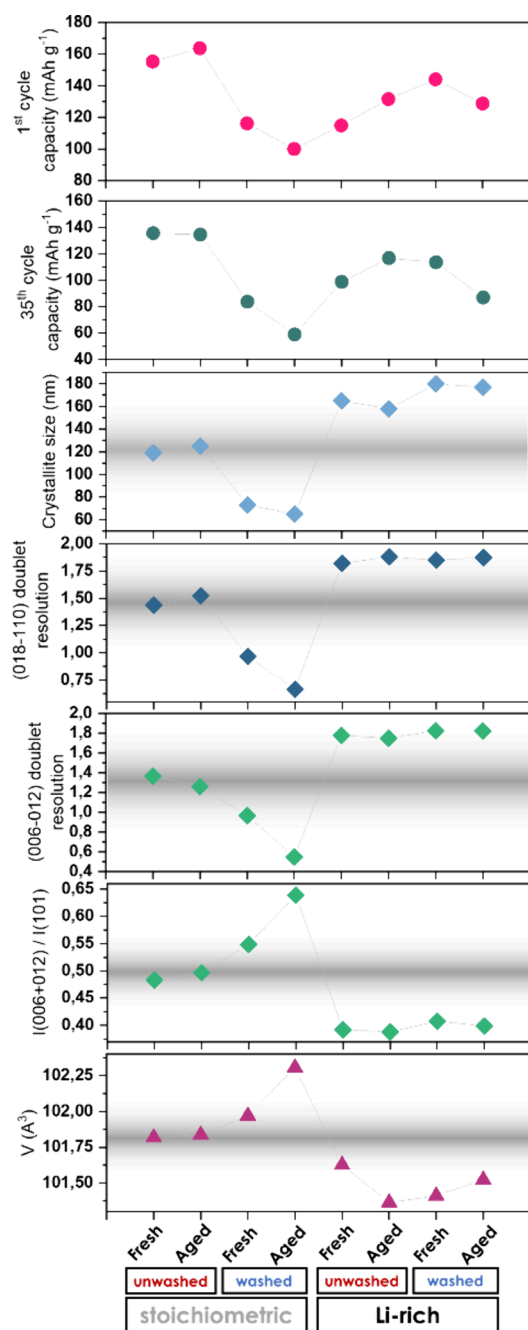
Figure 7. Comparison of structural parameters derived from XRD data through Rietveld refinement and electrochemical performance: unit cell volume V(Å^{-3}), intensity ratio of $I(006 + 012)/I(101)$, (006−012) and (018−110) doublets resolution, crystallite size (nm), and 35th and 1st discharge cycle capacities. Detailed parameters are presented in Table S6, pages S-13 (light gray lines are for eye-catching only).

A very similar trend to the doublet resolution and the crystal size was observed for the $I_{(006+012)}/I_{(101)}$ ratio. Analogously, we see the specific range in which this ratio represents samples with the best electrochemical performance, namely 0.47−0.53. As expected, above that upper value we see a dramatic decrease in discharge capacity.[109,111,113] Surprisingly, when that ratio is too low, we again see a worsening of the electrochemical behavior, which is in contradiction to the "as low as possible" value. A very low value of this ratio is connected to the fact that during the synthesis of Li-rich NMC811, the additional Li ions might incorporate into TM sites, lowering the (006) and (012) reflex intensities in the XRD pattern and thus the calculated ratio. If that is the case, then those Li-occupied TM sites become electrochemically inactive, consequently decreasing the specific capacity of the material.

The fourth comparable factor is the unit cell volume, which is characterized by a trend similar to that of the $I_{(006+012)}/I_{(101)}$ ratio. Here, the optimal value is ca. 101.8−101.83 Å^3. A bigger volume represents samples with disordered hexagonal structures (ST-NMC811-W and ST-NMC811-WA), whereas too small volumes correlate with all LR-NMC811 samples, which present unsatisfying electrochemical behavior. As discussed, volumes smaller than optimum indicate the excess Li occupation in TM sites (additionally to their 3b positions), whereas the volume expansion reveals the cation mixing. It is worth mentioning that analyzing the values of a and c unit parameters, they seem not to have a clear correlation with electrochemical behavior (Figure S10, page S-16). Although, looking closer at the a parameter, we can see some correlation. We think it can be an indicator of the preferable initial Li−Li distance (ca. 2.876 Å) for Li-ion hopping within the structure (⟨100⟩ and <010> directions) during the electrochemical process.

Few other parameters can be considered when correlating the electrochemical behavior of NMC811. From Figure S10 (page S-16), we see that the position of the (018) and (110) reflexes might hold important structural information. Especially, the (110) plane reflex is sensitive to electrochemical performance and the (110) plane distance needs to be of a particular value: in the case of NMC811, we assumed 1.44 Å. At the same time, the doublet (018)-(110) separation should be ca. 0.435, and c/3a ratio close to 1.648. Since the four selected parameters correlated more directly to electrochemical performance, we would recommend those in future studies. We also suggest that there are specific ranges for optimal parameters for specific NMC compositions, and they cannot be taken arbitrarily.

■ CONCLUSIONS

This study aimed to examine and explain the morphological surface transformation of stoichiometric and Li-rich NMC811 as a washing and aging consequence and link structural parameters to electrochemical analysis. The X-ray diffraction, SEM analysis, and Raman mapping were employed to identify the LRC and their postsynthetic and aging-related distribution. This comprehensive analysis was implemented for a Li-ion battery system with liquid electrolyte concerning the influence of detected LRC on the structure, morphology, and electrochemical performance. The LRC growth mechanism was proposed and linked to electrode preparation issues and overall cell performance. Our detailed examination of XRD doublets, and reflex intensity ratios through Rietveld analysis led us to the conclusion that four structural parameters can be chosen to

studied materials, $R_{(018-110)}$ should fit in between 1.4 and 1.6 and the crystal size of ca. 120 nm. From our calculations, we concluded that if the crystal size is too big, which manifest in smaller fwhm ($R_{(018-110)}$ > 1.7) or the doublet separation or crystal size are too small ($R_{(018-110)}$ < 1.1) the electrochemical performance will be affected. A doublet resolution of (006)-(012) reflexes ($R_{(006-012)}$) gives the same trend and also can be used for crystal evaluation if necessary. In this case the optimal values lie in between 1.5 and 1.2.

correlate the electrochemical performance with the crystal quality of NMC811: unit cell volume, intensity ratio $I_{(006+012)}/I_{(101)}$, crystal size, and newly introduced doublet resolution $R_{(018-110)}$. For this particular set of studied materials, the NMC811 crystal size should be ca. 120 nm, doublet resolution $R_{(018-110)}$ fit in between 1.4 and 1.6, with the optimal value of unit cell volume of ca. 101.8–101.83 $Å^3$, and intensity ratio $I_{(006+012)}/I_{(101)}$ in a range of 0.47–0.53. Meeting all four structural criteria could help to deduce the electrochemical performance of NMC. However, it is highly advised to set proper ranges individually for each NMC composition, since the indicated ranges are not described arbitrarily for the whole NMC family because the TM composition has a significant impact on the fundamental unit cell parameters and the arrangement of atoms within the structure, which consequently change the indirectly estimated values of $I_{(003)}/I_{(104)}$ calculated from XRD patterns.

■ ASSOCIATED CONTENT

ⓢ Supporting Information

The Supporting Information is available free of charge at https://pubs.acs.org/doi/10.1021/acsomega.4c06636.

Illustration of sample preparation, calcination, and washing procedure with further aging; Photographs of: (a) several electrode layers prepared from LR-NMC811 powder; (b) 4 mg of selected lithium compound in 5% PVdF in NMP preblend (0.5 g); (c) 1 wt % of selected lithium compound in NMP; Photographs of Li-rich NMC (a) just after the synthesis and (b) 9 months later with white deposits on the surface visible with the naked eye; SEM images of second-batch NMC811 samples: (a) and (b) stored in ambient air (different magnitudes); (c) and (d) stored in an Ar-filled glovebox for 9 months in an open jar and vacuum bag, respectively; XRD pattern for all NMC811 materials at the limited range of 2θ angle to highlight the most intense reflexes, their shapes, and positions; Rietveld refinement of powder XRD data collected for all NMC811 samples. All patterns showed good agreement with the $R\bar{3}m$ reference pattern. Sample ST-NMC811-W and ST-NMC811-WA also revealed a rock salt substructure of $Fm\bar{3}m$; Elemental composition of fresh samples evaluated by EDS in wt %; Elemental composition of fresh samples evaluated by ICP-MS in wt %; Elemental composition of fresh samples evaluated by ICP-MS in molar %; Refined lattice parameters for XRD patterns from Figure S5; Occupation of Wyckoff position by each element based on Rietveld refinement of fresh samples; Schematic representation of H_2O and CO_2 reactions with the NMC811, creating LRC at the surface; Structural models of the $C2/m$ monoclinic structure (stage III) of $LiOH \cdot H_2O$ showing multiple crystal facets: (201), (021), (20-1), and (11-1), which expose (220) planes that can create pathways for the reaction with CO_2 with OH^- groups; XRD patterns of the electrodes: fresh (as-prepared) and after C-rate tests; Electrochemical charge–discharge curves for the 1st, 5th, and 35th cycle of fresh and aged samples with calculated irreversible capacity loss in the first cycle; XRD-based crystallite size for all samples; and Comparison of structural parameters derived from XRD scans through Rietveld refinement (PDF)

■ AUTHOR INFORMATION

Corresponding Author

Dominika A. Buchberger − *Faculty of Chemistry, University of Warsaw, 02-093 Warsaw, Poland;* ⓞ orcid.org/0000-0001-7617-6991; Email: d.buchberger@uw.edu.pl

Authors

Magdalena Winkowska-Struzik − *Faculty of Chemistry, University of Warsaw, 02-093 Warsaw, Poland;* ⓞ orcid.org/0000-0003-4653-0958

Witold Uhrynowski − *Faculty of Chemistry, University of Warsaw, 02-093 Warsaw, Poland*

Michał Struzik − *Faculty of Physics, Warsaw University of Technology, 00-662 Warsaw, Poland; Centre for Advanced Materials and Technologies CEZAMAT, Warsaw University of Technology, 02-882 Warsaw, Poland;* ⓞ orcid.org/0000-0002-3086-469X

Andrzej Czerwinski − *Faculty of Chemistry, University of Warsaw, 02-093 Warsaw, Poland*

Complete contact information is available at:
https://pubs.acs.org/10.1021/acsomega.4c06636

Author Contributions

D.A.B. conceived the original idea, gained funding, and supervised the study. D.A.B. and M.W.-S. made important contributions to designing the study and interpreting the results. M.W.-S. performed the synthesis of NMC materials and arranged SEM experiments. W.U. arranged ICP-MS experiments. M.W.-S. and M.S. performed XRD measurements. D.A.B and M.W.-S. conducted structural and morphological data analyses. M.W.-S. performed electrochemical measurements and analyzed electrochemical data. D.A.B. performed Raman analysis and prepared crystallographic models of structures. M.W.-S. and D.A.B. wrote the manuscript and prepared visual graphs and tables. A.C. reviewed the final manuscript. All the authors revised and commented on the paper. All authors have approved the final version of the manuscript.

Notes

The authors declare no competing financial interest.

■ REFERENCES

(1) Li, J.; Downie, L. E.; Ma, L.; Qiu, W.; Dahn, J. R. Study of the Failure Mechanisms of LiNi 0.8 Mn 0.1 Co 0.1 O 2 Cathode Material for Lithium Ion Batteries. *J. Electrochem. Soc.* **2015**, *162* (7), A1401−A1408.

(2) Li, W.; Erickson, E. M.; Manthiram, A. High-Nickel Layered Oxide Cathodes for Lithium-Based Automotive Batteries. *Nat. Energy* **2020**, *5* (1), 26−34.

(3) Myung, S. T.; Maglia, F.; Park, K. J.; Yoon, C. S.; Lamp, P.; Kim, S. J.; Sun, Y. K. Nickel-Rich Layered Cathode Materials for Automotive Lithium-Ion Batteries: Achievements and Perspectives. *ACS Energy Lett.* **2017**, *2* (1), 196−223.

(4) Chen, Y.; Song, S.; Zhang, X.; Liu, Y. The Challenges, Solutions and Development of High Energy Ni-Rich NCM/NCA LiB Cathode Materials. *J. Phys. Conf. Ser.* **2019**, *1347* (1), 012012.

(5) Schipper, F.; Erickson, E. M.; Erk, C.; Shin, J.-Y.; Chesneau, F. F.; Aurbach, D. Review—Recent Advances and Remaining Challenges for Lithium Ion Battery Cathodes. *J. Electrochem. Soc.* **2017**, *164* (1), A6220−A6228.

(6) Shannon, R. D. Revised effective ionic radii and systematic studies of interatomic distances in halides and chalcogenides. *Acta Cryst. A* **1976**, *32*, 751.

(7) Zhang, X.; Jiang, W. J.; Mauger, A.; Qilu; Gendron, F.; Julien, C. M. Minimization of the Cation Mixing in Li1+x(NMC)1-XO2 as Cathode Material. *J. Power Sources* **2010**, *195* (5), 1292−1301.

(8) Cui, J.; Ding, X.; Luo, D.; Xie, H.; Zhang, Z.; Zhang, B.; Tan, F.; Liu, C.; Lin, Z. Effect of Cationic Uniformity in Precursors on Li/Ni Mixing of Ni-Rich Layered Cathodes. *Energy Fuels* **2021**, *35* (2), 1842−1850.

(9) Jung, R.; Strobl, P.; Maglia, F.; Stinner, C.; Gasteiger, H. A. Temperature Dependence of Oxygen Release from LiNi 0.6 Mn 0.2 Co 0.2 O 2 (NMC622) Cathode Materials for Li-Ion Batteries. *J. Electrochem. Soc.* **2018**, *165* (11), A2869−A2879.

(10) De Biasi, L.; Kondrakov, A. O.; Geßwein, H.; Brezesinski, T.; Hartmann, P.; Janek, J. Between Scylla and Charybdis: Balancing among Structural Stability and Energy Density of Layered NCM Cathode Materials for Advanced Lithium-Ion Batteries. *J. Phys. Chem. C* **2017**, *121* (47), 26163−26171.

(11) Jung, R.; Metzger, M.; Maglia, F.; Stinner, C.; Gasteiger, H. A. Oxygen Release and Its Effect on the Cycling Stability of LiNi x Mn y Co z O 2 (NMC) Cathode Materials for Li-Ion Batteries. *J. Electrochem. Soc.* **2017**, *164* (7), A1361−A1377.

(12) Dose, W. M.; Temprano, I.; Allen, J. P.; Björklund, E.; O'keefe, C. A.; Li, W.; Mehdi, B. L.; Weatherup, R. S.; De Volder, M. F. L.; Grey, C. P. Electrolyte Reactivity at the Charged Ni-Rich Cathode Interface and Degradation in Li-Ion Batteries. *Cite This: ACS Appl. Mater. Interfaces* **2022**, *14*, 13206−13222.

(13) Seong, W. M.; Kim, Y.; Manthiram, A. Impact of Residual Lithium on the Adoption of High-Nickel Layered Oxide Cathodes for Lithium-Ion Batteries. *Chem. Mater.* **2020**, *32* (22), 9479−9489.

(14) Zhang, L.; Müller Gubler, E. A.; Tai, C. W.; Kondracki, Ł.; Sommer, H.; Novák, P.; El Kazzi, M.; Trabesinger, S. Elucidating the Humidity-Induced Degradation of Ni-Rich Layered Cathodes for Li-Ion Batteries. *ACS Appl. Mater. Interfaces* **2022**, *14* (11), 13240−13249.

(15) Renfrew, S. E.; McCloskey, B. D. Residual Lithium Carbonate Predominantly Accounts for First Cycle CO2 and CO Outgassing of Li-Stoichiometric and Li-Rich Layered Transition-Metal Oxides. *J. Am. Chem. Soc.* **2017**, *139* (49), 17853−17860.

(16) Kaufman, L. A.; McCloskey, B. D. Surface Lithium Carbonate Influences Electrolyte Degradation via Reactive Oxygen Attack in Lithium-Excess Cathode Materials. *Chem. Mater.* **2021**, *33* (11), 4170−4176.

(17) Hartmann, L.; Pritzl, D.; Beyer, H.; Gasteiger, H. A. Evidence for Li + /H + Exchange during Ambient Storage of Ni-Rich Cathode Active Materials. *J. Electrochem. Soc.* **2021**, *168* (7), 070507.

(18) Seong, W. M.; Cho, K.-H.; Park, J.-W.; Park, H.; Eum, D.; Lee, M. H.; Kim, I.-s. S.; Lim, J.; Kang, K. Controlling Residual Lithium in High-Nickel ('90%) Lithium Layered Oxides for Cathodes in Lithium-Ion Batteries. *Angewandte Chemie - International Edition* **2020**, *59* (42), 18662−18669.

(19) Nohma, T.; Kurokawa, H.; Uehara, M.; Takahashi, M.; Nishio, K.; Saito, T. Electrochemical Characteristics of LiNiO2 and LiCoO2 as Positive Material for Lithium Secondary Batteries. *J. Power Sources* **1995**, *54*, 522−524.

(20) Hamam, I.; Zhang, N.; Liu, A.; Johnson, M. B.; Dahn, J. R. Study of the Reactions between Ni-Rich Positive Electrode Materials and Aqueous Solutions and Their Relation to the Failure of Li-Ion Cells. *J. Electrochem. Soc.* **2020**, *167* (13), 130521.

(21) Kim, Y.; Park, H.; Warner, J. H.; Manthiram, A. Unraveling the Intricacies of Residual Lithium in High-Ni Cathodes for Lithium-Ion Batteries. *ACS Energy Lett.* **2021**, *6* (3), 941−948.

(22) Bi, Y.; Li, Q.; Yi, R.; Xiao, J. To Pave the Way for Large-Scale Electrode Processing of Moisture-Sensitive Ni-Rich Cathodes. *J. Electrochem. Soc.* **2022**, *169* (2), 020521.

(23) Shizuka, K.; Kiyohara, C.; Shima, K.; Takeda, Y. Effect of CO2 on Layered Li1+zNi1-x-YCoxMyO2 (M = Al, Mn) Cathode Materials for Lithium Ion Batteries. *J. Power Sources* **2007**, *166* (1), 233−238.

(24) Fang, Z.; Confer, M. P.; Wang, Y.; Wang, Q.; Kunz, M. R.; Dufek, E. J.; Liaw, B.; Klein, T. M.; Dixon, D. A.; Fushimi, R. Formation of Surface Impurities on Lithium-Nickel-Manganese-Cobalt Oxides in the Presence of CO2and H2O. *J. Am. Chem. Soc.* **2021**, *143* (27), 10261−10274.

(25) Shkrob, I. A.; Gilbert, J. A.; Phillips, P. J.; Klie, R.; Haasch, R. T.; Bareño, J.; Abraham, D. P. Chemical Weathering of Layered Ni-Rich Oxide Electrode Materials: Evidence for Cation Exchange. *J. Electrochem. Soc.* **2017**, *164* (7), A1489−A1498.

(26) Pimenta, V.; Sathiya, M.; Batuk, D.; Abakumov, A. M.; Giaume, D.; Cassaignon, S.; Larcher, D.; Tarascon, J. M. Synthesis of Li-Rich NMC: A Comprehensive Study. *Chem. Mater.* **2017**, *29* (23), 9923−9936.

(27) Moshtev, R.; Zlatilova, P.; Vasilev, S.; Bakalova, I.; Kozawa, A. Synthesis, XRD Characterization and Electrochemical Performance of Overlithiated LiNiO2. *J. Power Sources* **1999**, *81−82*, 434−441.

(28) Yamada, S.; Fujiwara, M.; Kanda, M. Synthesis and properties of LiNiO2 as cathode material for secondary batteries. *Journal of Power Sources* **1995**, *54*, 209.

(29) Rathore, D.; Liang, C.; Zsoldos, E.; Ball, M.; Yu, S.; Yang, C.; Wang, Q.; Dahn, J. R. Elucidating the Role of Excess Li in the Electrochemical Performance of Li 1+x [Ni 0.5 Mn 0.5] 1-x O 2 Layered Oxides. *J. Electrochem. Soc.* **2023**, *170* (2), 020520.

(30) Dahn, J. R.; Von Sacken, U.; Michal, C. A. Structure and Electrochemistry of Li(1-x)NiO2 and a New Li2Ni02 Phase with the Ni(OH)2 Structure. *Solid State Ion* **1990**, *44*, 87−97.

(31) Arai, H.; Okada, S.; Ohtsuka, H.; Ichimura, M.; Yamaki, J. Characterization and Cathode Performance of Li1 - XNi1 + XO2 Prepared with the Excess Lithium Method. *Solid State Ion* **1995**, *80* (3−4), 261−269.

(32) Zhang, L.; Wang, X.; Muta, T.; Li, D.; Noguchi, H.; Yoshio, M.; Ma, R.; Takada, K.; Sasaki, T. The Effects of Extra Li Content, Synthesis Method, Sintering Temperature on Synthesis and Electrochemistry of Layered LiNi1/3Mn1/3Co1/3O2. *J. Power Sources* **2006**, *162* (1), 629−635.

(33) Paulsen, J.; Kim, J. H. High Nickel Cathode Material Having Low Soluble Base Content. US Patent 2014/0054495 A1, 2014.

(34) Cho, D.-H.; Jo, C.-H.; Cho, W.; Kim, Y.-J.; Yashiro, H.; Sun, Y.-K.; Myung, S.-T. Effect of Residual Lithium Compounds on Layer Ni-Rich Li[Ni 0.7 Mn 0.3]O 2. *J. Electrochem. Soc.* **2014**, *161* (6), A920−A926.

(35) Renfrew, S. E.; McCloskey, B. D. Residual Lithium Carbonate Predominantly Accounts for First Cycle CO2 and CO Outgassing of Li-Stoichiometric and Li-Rich Layered Transition-Metal Oxides. *J. Am. Chem. Soc.* **2017**, *139* (49), 17853−17860.

(36) Freiberg, A. T. S.; Sicklinger, J.; Solchenbach, S.; Gasteiger, H. A. Li2CO3 Decomposition in Li-Ion Batteries Induced by the Electrochemical Oxidation of the Electrolyte and of Electrolyte Impurities. *Electrochim. Acta* **2020**, *346*, 136271.

(37) Han, Y.; Lei, Y.; Ni, J.; Zhang, Y.; Geng, Z.; Ming, P.; Zhang, C.; Tian, X.; Shi, J. L.; Guo, Y. G.; Xiao, Q. Single-Crystalline Cathodes for Advanced Li-Ion Batteries: Progress and Challenges. *Small* **2022**, *18* (43), 2107048.

(38) Wang, T.; Ren, K.; He, M.; Dong, W.; Xiao, W.; Pan, H.; Yang, J.; Yang, Y.; Liu, P.; Cao, Z.; Ma, X.; Wang, H. Synthesis and Manipulation of Single-Crystalline Lithium Nickel Manganese Cobalt Oxide Cathodes: A Review of Growth Mechanism. *Frontiers in Chemistry* **2020**, *8*, 747.

(39) Fan, X.; Liu, Y.; Ou, X.; Zhang, J.; Zhang, B.; Wang, D.; Hu, G. Unravelling the Influence of Quasi Single-Crystalline Architecture on High-Voltage and Thermal Stability of LiNi0.5Co0.2Mn0.3O2 Cathode for Lithium-Ion Batteries. *Chemical Engineering Journal* **2020**, *393*, 124709.

(40) Oswald, S.; Bock, M.; Gasteiger, H. A. Elucidating the Implications of Morphology on Fundamental Characteristics of Nickel-Rich NCMs: Cracking, Gassing, Rate Capability, and Thermal Stability of Poly- and Single-Crystalline NCM622. *J. Electrochem. Soc.* **2022**, *169* (5), 050501.

(41) Ruess, R.; Ulherr, M. A.; Trevisanello, E.; Schröder, S.; Henss, A.; Janek, J. Transition Metal Oxides and Li 2 CO 3 as Precursors for the Synthesis of Ni-Rich Single-Crystalline NCM for Sustainable Lithium-Ion Battery Production. *J. Electrochem. Soc.* **2022**, *169* (7), 070531.

(42) Zhu, J.; Chen, G. Single-Crystal Based Studies for Correlating the Properties and High-Voltage Performance of Li[NixMnyCo1-x-y]O2 Cathodes. *J. Mater. Chem. A Mater.* **2019**, *7* (10), 5463−5474.

(43) Garayt, M. D. L.; Zhang, N.; Yu, S.; Abraham, J. J.; Murphy, A.; Omessi, R.; Ye, Z.; Azam, S.; Johnson, M. B.; Yang, C.; Dahn, J. R. Single Crystal Li 1+x [Ni 0.6 Mn 0.4] 1-x O 2 Made by All-Dry Synthesis. *J. Electrochem. Soc.* **2023**, *170* (6), 060529.

(44) Li, J.; Cameron, A. R.; Li, H.; Glazier, S.; Xiong, D.; Chatzidakis, M.; Allen, J.; Botton, G. A.; Dahn, J. R. Comparison of Single Crystal and Polycrystalline LiNi 0.5 Mn 0.3 Co 0.2 O 2 Positive Electrode Materials for High Voltage Li-Ion Cells. *J. Electrochem. Soc.* **2017**, *164* (7), A1534−A1544.

(45) Li, J.; Li, H.; Stone, W.; Weber, R.; Hy, S.; Dahn, J. R. Synthesis of Single Crystal LiNi 0.5 Mn 0.3 Co 0.2 O 2 for Lithium Ion Batteries. *J. Electrochem. Soc.* **2017**, *164* (14), A3529−A3537.

(46) Li, H.; Li, J.; Ma, X.; Dahn, J. R. Synthesis of Single Crystal LiNi 0.6 Mn 0.2 Co 0.2 O 2 with Enhanced Electrochemical Performance for Lithium Ion Batteries. *J. Electrochem. Soc.* **2018**, *165* (5), A1038−A1045.

(47) Li, J.; Cameron, A. R.; Li, H.; Glazier, S.; Xiong, D.; Chatzidakis, M.; Allen, J.; Botton, G. A.; Dahn, J. R. Comparison of Single Crystal and Polycrystalline LiNi 0.5 Mn 0.3 Co 0.2 O 2 Positive Electrode Materials for High Voltage Li-Ion Cells. *J. Electrochem. Soc.* **2017**, *164* (7), A1534−A1544.

(48) Chen, Z.; Dahn, J. R. Methods to Obtain Excellent Capacity Retention in LiCoO2 Cycled to 4.5 V. *Electrochim. Acta* **2004**, *49* (7), 1079−1090.

(49) Langdon, J.; Manthiram, A. A Perspective on Single-Crystal Layered Oxide Cathodes for Lithium-Ion Batteries. *Energy Storage Mater.* **2021**, *37*, 143−160.

(50) Aiken, C. P.; Logan, E. R.; Eldesoky, A.; Hebecker, H.; Oxner, J. M.; Harlow, J. E.; Metzger, M.; Dahn, J. R. Li[Ni 0.5 Mn 0.3 Co 0.2]O 2 as a Superior Alternative to LiFePO 4 for Long-Lived Low Voltage Li-Ion Cells. *J. Electrochem. Soc.* **2022**, *169* (5), 050512.

(51) Harlow, J. E.; Ma, X.; Li, J.; Logan, E.; Liu, Y.; Zhang, N.; Ma, L.; Glazier, S. L.; Cormier, M. M. E.; Genovese, M.; Buteau, S.; Cameron, A.; Stark, J. E.; Dahn, J. R. A Wide Range of Testing Results on an Excellent Lithium-Ion Cell Chemistry to Be Used as Benchmarks for New Battery Technologies. *J. Electrochem. Soc.* **2019**, *166* (13), A3031−A3044.

(52) Han, Y.; Lei, Y.; Ni, J.; Zhang, Y.; Geng, Z.; Ming, P.; Zhang, C.; Tian, X.; Shi, J. L.; Guo, Y. G.; Xiao, Q. Single-Crystalline Cathodes for Advanced Li-Ion Batteries: Progress and Challenges. *Small* **2022**, *18* (43), 2107048.

(53) Zhang, N.; Yu, H.; Murphy, A.; Garayt, M.; Yu, S.; Rathore, D.; Leontowich, A.; Bond, T.; Kim, C.-Y.; Dahn, J. R. A Liquid and Waste-Free Method for Preparing Single Crystal Positive Electrode Materials for Li-Ion Batteries. *J. Electrochem. Soc.* **2023**, *170* (7), 070515.

(54) Chen, Z.; Dahn, J. R. Methods to Obtain Excellent Capacity Retention in LiCoO2 Cycled to 4.5 V. *Electrochim. Acta* **2004**, *49* (7), 1079−1090.

(55) Laurita, A.; Zhu, L.; Cabelguen, P. E.; Auvergniot, J.; Hamon, J.; Guyomard, D.; Dupré, N.; Moreau, P. Pristine Surface of Ni-Rich Layered Transition Metal Oxides as a Premise of Surface Reactivity. *ACS Appl. Mater. Interfaces* **2022**, *14* (37), 41945−41956.

(56) Chen, A.; Wang, K.; Li, J.; Mao, Q.; Xiao, Z.; Zhu, D.; Wang, G.; Liao, P.; He, J.; You, Y.; Xia, Y. The Formation, Detriment and

Solution of Residual Lithium Compounds on Ni-Rich Layered Oxides in Lithium-Ion Batteries. *Front Energy Res.* **2020**, *8*, 1−16.

(57) Seong, W. M.; Kim, Y.; Manthiram, A. Impact of Residual Lithium on the Adoption of High-Nickel Layered Oxide Cathodes for Lithium-Ion Batteries. *Chem. Mater.* **2020**, *32* (22), 9479−9489.

(58) Kim, Y.; Park, H.; Warner, J. H.; Manthiram, A. Unraveling the Intricacies of Residual Lithium in High-Ni Cathodes for Lithium-Ion Batteries. *ACS Energy Lett.* **2021**, *6* (3), 941−948.

(59) Seong, W. M.; Cho, K.; Park, J.; Park, H.; Eum, D.; Lee, M. H.; Kim, I. S.; Lim, J.; Kang, K. Controlling Residual Lithium in High-Nickel (>90%) Lithium Layered Oxides for Cathodes in Lithium-Ion Batteries. *Angew. Chem., Int. Ed.* **2020**, *59* (42), 18662−18669.

(60) Jung, R.; Morasch, R.; Karayaylali, P.; Phillips, K.; Maglia, F.; Stinner, C.; Shao-Horn, Y.; Gasteiger, H. A. Effect of Ambient Storage on the Degradation of Ni-Rich Positive Electrode Materials (NMC811) for Li-Ion Batteries. *J. Electrochem. Soc.* **2018**, *165* (2), A132−A141.

(61) Busà, C.; Belekoukia, M.; Loveridge, M. J. The Effects of Ambient Storage Conditions on the Structural and Electrochemical Properties of NMC-811 Cathodes for Li-Ion Batteries. *Electrochim. Acta* **2021**, *366*, 137358.

(62) Marshall, J. E.; Zhenova, A.; Roberts, S.; Petchey, T.; Zhu, P.; Dancer, C. E. J.; McElroy, C. R.; Kendrick, E.; Goodship, V. On the Solubility and Stability of Polyvinylidene Fluoride. *Polymers (Basel)* **2021**, *13* (9), 1354.

(63) Roberts, S.; Chen, L.; Kishore, B.; Dancer, C. E. J.; Simmons, M. J. H.; Kendrick, E. Mechanism of Gelation in High Nickel Content Cathode Slurries for Sodium-Ion Batteries. *J. Colloid Interface Sci.* **2022**, *627*, 427−437.

(64) Song, G.; Lin, Y.; Zhu, Z.; Zheng, H.; Qiao, J.; He, C.; Wang, H. Strong Fluorescence of Poly (N-Vinylpyrrolidone) and Its Oxidized Hydrolyzate. *Macromol. Rapid Commun.* **2015**, *36* (3), 278−285.

(65) Zima, T. M.; Vorsina, I. A.; Lyakhov, N. Z. Interaction of Poly-N-Vinylpyrrolidone with Hydrated Metal Oxides. *Inorg. Mater.* **2009**, *45* (5), 524−532.

(66) Yin, M.; Ye, Y.; Sun, M.; Kang, N.; Yang, W. Facile One-Pot Synthesis of a Polyvinylpyrrolidone-Based Self-Crosslinked Fluorescent Film. *Macromol. Rapid Commun.* **2013**, *34* (7), 616−620.

(67) Heck, C. A.; Huttner, F.; Mayer, J. K.; Fromm, O.; Börner, M.; Heckmann, T.; Scharfer, P.; Schabel, W.; Winter, M.; Kwade, A. Production of Nickel-Rich Cathodes for Lithium-Ion Batteries from Lab to Pilot Scale under Investigation of the Process Atmosphere. *Energy Technology* **2023**, *11*, 2200945.

(68) Seong, W. M.; Kim, Y.; Manthiram, A. Impact of Residual Lithium on the Adoption of High-Nickel Layered Oxide Cathodes for Lithium-Ion Batteries. *Chem. Mater.* **2020**, *32*, 9479−9489.

(69) Zhang, W.; Yuan, C.; Zhu, J.; Jin, T.; Shen, C.; Xie, K. Air Instability of Ni-Rich Layered Oxides-A Roadblock to Large Scale Application. *Advanced Energy Materials* **2023**, *13* (2), 2202993.

(70) Herzog, M. J.; Esken, D.; Janek, J. Improved Cycling Performance of High-Nickel NMC by Dry Powder Coating with Nanostructured Fumed Al2O3, TiO2, and ZrO2: A Comparison. *Batter Supercaps* **2021**, *4* (6), 1003−1017.

(71) Moryson, Y.; Walther, F.; Sann, J.; Mogwitz, B.; Ahmed, S.; Burkhardt, S.; Chen, L.; Klar, P. J.; Volz, K.; Fearn, S.; Rohnke, M.; Janek, J. Analyzing Nanometer-Thin Cathode Particle Coatings for Lithium-Ion Batteries—The Example of TiO 2 on NCM622. *ACS Appl. Energy Mater.* **2021**, *4* (7), 7168−7181.

(72) Chung, Y.; Shin, Y.; Liu, Y.; Park, J. S.; Margez, C. L.; Greszler, T. A. Synergetic Effect of Carbon and AlF 3 Coatings on the Lithium Titanium Oxide Anode Material for High Power Lithium-Ion Batteries. *J. Electroanal. Chem.* **2019**, *837*, 240−245.

(73) Ahaliabadeh, Z.; Kong, X.; Fedorovskaya, E.; Kallio, T. Extensive Comparison of Doping and Coating Strategies for Ni-Rich Positive Electrode Materials. *J. Power Sources* **2022**, *540*, 231633.

(74) Gao, Y.; Park, J.; Liang, X. Comprehensive Study of Al- And Zr-Modified LiNi0.8Mn0.1Co0.1O2through Synergy of Coating and Doping. *ACS Appl. Energy Mater.* **2020**, *3* (9), 8978−8987.

(75) Makhonina, E. V.; Maslennikova, L. S.; Volkov, V. V.; Medvedeva, A. E.; Rumyantsev, A. M.; Koshtyal, Y. M.; Maximov, M. Y.; Pervov, V. S.; Eremenko, I. L. Li-Rich and Ni-Rich Transition Metal Oxides: Coating and Core-Shell Structures. *Appl. Surf. Sci.* **2019**, *474*, 25−33.

(76) Darbar, D.; Self, E. C.; Li, L.; Wang, C.; Meyer, H. M.; Lee, C.; Croy, J. R.; Balasubramanian, M.; Muralidharan, N.; Bhattacharya, I.; Belharouak, I.; Nanda, J. New Synthesis Strategies to Improve Co-Free LiNi0.5Mn0.5O2 Cathodes: Early Transition Metal D0 Dopants and Manganese Pyrophosphate Coating. *J. Power Sources* **2020**, *479*, 228591.

(77) Weber, D.; Tripković, Đ.; Kretschmer, K.; Bianchini, M.; Brezesinski, T. Surface Modification Strategies for Improving the Cycling Performance of Ni-Rich Cathode Materials. *Eur. J. Inorg. Chem.* **2020**, *2020* (33), 3117−3130.

(78) Kim, J.; Hong, Y.; Ryu, K. S.; Kim, M. G.; Cho, J. Washing Effect of a LiNi0.83Co0.15Al 0.02O2 Cathode in Water. *Electrochem. Solid-State Lett.* **2006**, *9* (1), A19−A23.

(79) LIU, W.-m.; QIN, M.-l.; XU, L.; YI, S.; DENG, J.-y.; HUANG, Z.-h. Washing Effect on Properties of LiNi0.8Co0.15Al0.05O2 Cathode Material by Ethanol Solvent. *Transactions of Nonferrous Metals Society of China (English Edition)* **2018**, *28* (8), 1626−1631.

(80) Xiong, X.; Wang, Z.; Yue, P.; Guo, H.; Wu, F.; Wang, J.; Li, X. Washing Effects on Electrochemical Performance and Storage Characteristics of LiNi0.8Co0.1Mn0.1O2 as Cathode Material for Lithium-Ion Batteries. *J. Power Sources* **2013**, *222*, 318−325.

(81) Hartmann, L.; Ching, C. H.; Kipfer, T.; Koch, M.; Gasteiger, H. A. Surface-Stabilization of LMR-NCM by Washing with Aqueous Buffers to Reduce Gassing and Improve Cycle-Life. *J. Electrochem. Soc.* **2022**, *169* (7), 070516.

(82) Hartmann, L.; Ching, C. H.; Kipfer, T.; Koch, M.; Gasteiger, H. A. Surface-Stabilization of LMR-NCM by Washing with Aqueous Buffers to Reduce Gassing and Improve Cycle-Life. *J. Electrochem. Soc.* **2022**, *169* (7), 070516.

(83) Lee, W.; Lee, D.; Kim, Y.; Choi, W.; Yoon, W. S. Enhancing the Structural Durability of Ni-Rich Layered Materials by Post-Process: Washing and Heat-Treatment. *J. Mater. Chem. A Mater.* **2020**, *8* (20), 10206−10216.

(84) Xiong, X.; Wang, Z.; Yue, P.; Guo, H.; Wu, F.; Wang, J.; Li, X. Washing Effects on Electrochemical Performance and Storage Characteristics of LiNi0.8Co0.1Mn0.1O2 as Cathode Material for Lithium-Ion Batteries. *J. Power Sources* **2013**, *222*, 318−325.

(85) Pritzl, D.; Teufl, T.; Freiberg, A. T. S.; Strehle, B.; Sicklinger, J.; Sommer, H.; Hartmann, P.; Gasteiger, H. A. Editors' Choice—Washing of Nickel-Rich Cathode Materials for Lithium-Ion Batteries: Towards a Mechanistic Understanding. *J. Electrochem. Soc.* **2019**, *166* (16), A4056−A4066.

(86) Shin, J.-S.; Han, C.-H.; Jung, U.-H.; Lee, S.-I.; Kim, H.-J.; Kim, K. Effect of Li2CO3 Additive on Gas Generation in Lithium-Ion Batteries. *J. Power Sources* **2002**, *109* (1), 47−52.

(87) Klein, S.; Harte, P.; Henschel, J.; Bärmann, P.; Borzutzki, K.; Beuse, T.; van Wickeren, S.; Heidrich, B.; Kasnatscheew, J.; Nowak, S.; Winter, M.; Placke, T. On the Beneficial Impact of Li2CO3 as Electrolyte Additive in NCM523 ∥ Graphite Lithium Ion Cells Under High-Voltage Conditions. *Adv. Energy Mater.* **2021**, *11* (10), 2003756.

(88) Mahne, N.; Renfrew, S. E.; McCloskey, B. D.; Freunberger, S. A. Elektrochemische Oxidation von Lithiumcarbonat Generiert Singulett-Sauerstoff. *Angew. Chem.* **2018**, *130* (19), 5627−5631.

(89) Kim, J.; Kim, O.; Park, C.; Lee, G.; Shin, D. Electrochemical Properties of Li 1+x CoO 2 Synthesized for All-Solid-State Lithium Ion Batteries with Li 2 S-P 2 S 5 Glass-Ceramics Electrolyte. *J. Electrochem. Soc.* **2015**, *162* (6), A1041−A1045.

(90) Sheng, H.; Meng, X. H.; Xiao, D. D.; Fan, M.; Chen, W. P.; Wan, J.; Tang, J.; Zou, Y. G.; Wang, F.; Wen, R.; Shi, J. L.; Guo, Y. G. An Air-Stable High-Nickel Cathode with Reinforced Electrochemical Performance Enabled by Convertible Amorphous Li2CO3Modification. *Adv. Mater.* **2022**, *34* (12), 2108947.

(91) Li, J.; Zhong, W.; Deng, Q.; Zhang, Q.; Yang, C. Recent Progress in Synthesis and Surface Modification of Nickel-Rich

(92) Ding, Y.; Mu, D.; Wu, B.; Zhao, Z.; Wang, R. Controllable Synthesis of Spherical Precursor Ni0.8Co0.1Mn0.1(OH)2 for Nickel-Rich Cathode Material in Li-Ion Batteries. *Ceram. Int.* **2020**, *46* (7), 9436−9445.

(93) Wang, T.; Ren, K.; He, M.; Dong, W.; Xiao, W.; Pan, H.; Yang, J.; Yang, Y.; Liu, P.; Cao, Z.; Ma, X.; Wang, H. Synthesis and Manipulation of Single-Crystalline Lithium Nickel Manganese Cobalt Oxide Cathodes: A Review of Growth Mechanism. *Front Chem.* **2020**, *8*, 1−8.

(94) Ruess, R.; Gomboso, D.; Ulherr, M. A.; Trevisanello, E.; Ma, Y.; Kondrakov, A.; Brezesinski, T.; Janek, J. Single-Crystalline LiNiO 2 as High-Capacity Cathode Active Material for Solid-State Lithium-Ion Batteries. *J. Electrochem. Soc.* **2023**, DOI: 10.1149/1945-7111/acbc4f.

(95) Payandeh, S.; Goonetilleke, D.; Bianchini, M.; Janek, J.; Brezesinski, T. Single versus Poly-Crystalline Layered Oxide Cathode Materials for Solid-State Battery Applications - a Short Review Article. *Curr. Opin Electrochem* **2022**, *31*, 100877.

(96) Dinh, L. N.; McLean, W.; Schildbach, M. A.; LeMay, J. D.; Siekhaus, W. J.; Balooch, M. The Nature and Effects of the Thermal Stability of Lithium Hydroxide. *J. Nucl. Mater.* **2003**, *317* (2−3), 175−188.

(97) Fang, Z.; Confer, M. P.; Wang, Y.; Wang, Q.; Kunz, M. R.; Dufek, E. J.; Liaw, B.; Klein, T. M.; Dixon, D. A.; Fushimi, R. Formation of Surface Impurities on Lithium-Nickel-Manganese-Cobalt Oxides in the Presence of CO2and H2O. *J. Am. Chem. Soc.* **2021**, *143* (27), 10261−10274.

(98) Li, W.; Reimers, J. N.; Dahn, J. R. In Situ X-Ray Diffraction and Electrochemical Studies of Li1-XNiO2. *Solid State Ion* **1993**, *67* (1−2), 123−130.

(99) Arai, H.; Tsuda, M.; Sakurai, Y. *Lithium Nickelate Electrodes with Enhanced High-Temperature Performance and Thermal Stability*; 2000; Vol. 90. www.elsevier.comrlocaterjpowsour.

(100) Matsumoto, K.; Kuzuo, R.; Takeya, K.; Yamanaka, A. Effects of CO2 in Air on Li Deintercalation from LiNi1-x-YCoxAlyO2. *J. Power Sources* **1999**, *81−82*, 558−561.

(101) Greil, R.; Chai, J.; Rudelstorfer, G.; Mitsche, S.; Lux, S. Water as a Sustainable Leaching Agent for the Selective Leaching of Lithium from Spent Lithium-Ion Batteries. *ACS Omega* **2024**, DOI: 10.1021/acsomega.3c07405.

(102) Morales, J.; Pérez-Vicente, C.; Tirado, J. L. Cation Distribution and Chemical Deintercalation of Li1-XNi1+xO2. *Mater. Res. Bull.* **1990**, *25* (5), 623−630.

(103) Sieber, T.; Ducke, J.; Rietig, A.; Langner, T.; Acker, J. Recovery of Li(Ni0.33mn0.33co0.33)O2 from Lithium-Ion Battery Cathodes: Aspects of Degradation. *Nanomaterials* **2019**, *9* (2), 246.

(104) Gittleson, F. S.; Ryu, W. H.; Taylor, A. D. Operando Observation of the Gold-Electrolyte Interface in Li-O2 Batteries. *ACS Appl. Mater. Interfaces* **2014**, *6* (21), 19017−19025.

(105) Flores, E.; Novák, P.; Aschauer, U.; Berg, E. J. Cation Ordering and Redox Chemistry of Layered Ni-Rich Li XNi1−2 YCo YMn YO2: An Operando Raman Spectroscopy Study. *Chem. Mater.* **2020**, *32* (1), 186−194.

(106) Williams, D. D.; Miller, R. R. Effect of Water Vapor on the LiOH-CO2 Reaction. Dynamic Isothermal System. *Industrial & Engineering Chemistry Fundamentals* **1970**, *9* (3), 454−457.

(107) Billy, E.; Joulié, M.; Laucournet, R.; Boulineau, A.; De Vito, E.; Meyer, D. Dissolution Mechanisms of LiNi1/3Mn1/3Co1/3O2 Positive Electrode Material from Lithium-Ion Batteries in Acid Solution. *ACS Appl. Mater. Interfaces* **2018**, *10* (19), 16424−16435.

(108) Ohzuku, T.; Ueda, A.; Nagayama, M. Electrochemistry and Structural Chemistry of LiNiO2 (R3m) for 4 V Secondary Lithium Cells. *J. Electrochem. Soc.* **1993**, *140* (7), 1862.

(109) Zhang, X.; Jiang, W. J.; Mauger, A.; Qilu; Gendron, F.; Julien, C. M. Minimization of the Cation Mixing in Li1+x(NMC)1-XO2 as Cathode Material. *J. Power Sources* **2010**, *195* (5), 1292−1301.

(110) Ohzuku, T.; Ueda, A.; Nagayama, M.; Iwakoshi, Y.; Komori, H. COMPARATIVE STUDY OF LiCoO2, LiNi1/2Co1/2O2 AND LiNiO2 FOR 4 VOLT SECONDARY. *Electrochim. Acta* **1993**, *38* (9), 1159.

(111) Julien, C.; Mauger, A.; Zaghib, K.; Groult, H. Optimization of Layered Cathode Materials for Lithium-Ion Batteries. *Materials* **2016**, *9* (7), 595.

(112) Julien, C. M.; Mauger, A.; Zaghib, K.; Groult, H. Comparative Issues of Cathode Materials for Li-Ion Batteries. *Inorganics (Basel)* **2014**, *2* (1), 132−154.

(113) Ben-Kamel, K.; Amdouni, N.; Mauger, A.; Julien, C. M. Study of the Local Structure of LiNi $0.33+\delta$ Mn $0.33+\delta$ Co $0.33−2\delta$ O 2 $(0.025 \leq \delta \leq 0.075)$ Oxides. *J. Alloys Compd.* **2012**, *528*, 91−98.

(114) Cui, J.; Ding, X.; Luo, D.; Xie, H.; Zhang, Z.; Zhang, B.; Tan, F.; Liu, C.; Lin, Z. Effect of Cationic Uniformity in Precursors on Li/Ni Mixing of Ni-Rich Layered Cathodes. *Energy Fuels* **2021**, *35* (2), 1842−1850.

(115) Lu, Z.; MacNeil, D. D.; Dahn, J. R. Layered Li[NixCo1−2xMnx]O2 Cathode Materials for Lithium-Ion Batteries. *Electrochem. Solid-State Lett.* **2001**, *4* (12), A200.

(116) Li, J.; Yao, R.; Cao, C. LiNi1/3Co1/3Mn1/3O2 Nanoplates with {010} Active Planes Exposing Prepared in Polyol Medium as a High-Performance Cathode for Li-Ion Battery. *ACS Appl. Mater. Interfaces* **2014**, *6* (7), 5075−5082.

(117) Zhang, L.; Li, N.; Wu, B.; Xu, H.; Wang, L.; Yang, X. Q.; Wu, F. Sphere-Shaped Hierarchical Cathode with Enhanced Growth of Nanocrystal Planes for High-Rate and Cycling-Stable Li-Ion Batteries. *Nano Lett.* **2015**, *15* (1), 656−661.

(118) Xu, M.; Fei, L.; Zhang, W.; Li, T.; Lu, W.; Zhang, N.; Lai, Y.; Zhang, Z.; Fang, J.; Zhang, K.; Li, J.; Huang, H. Tailoring Anisotropic Li-Ion Transport Tunnels on Orthogonally Arranged Li-Rich Layered Oxide Nanoplates Toward High-Performance Li-Ion Batteries. *Nano Lett.* **2017**, *17* (3), 1670−1677.

(119) Märker, K.; Reeves, P. J.; Xu, C.; Griffith, K. J.; Grey, C. P. Evolution of Structure and Lithium Dynamics in LiNi0.8Mn0.1-Co0.1O2 (NMC811) Cathodes during Electrochemical Cycling. *Chem. Mater.* **2019**, *31* (7), 2545−2554.

(120) Li, Y.; Bai, Y.; Wu, C.; Qian, J.; Chen, G.; Liu, L.; Wang, H.; Zhou, X.; Wu, F. Three-Dimensional Fusiform Hierarchical Micro/Nano Li1.2Ni0.2Mn0.6O2 with a Preferred Orientation (110) Plane as a High Energy Cathode Material for Lithium-Ion Batteries. *J. Mater. Chem. A Mater.* **2016**, *4* (16), 5942−5951.

(121) Chen, M.; Jin, X.; Chen, Z.; Zhong, Y.; Liao, Y.; Qiu, Y.; Cao, G.; Li, W. A Cross-like Hierarchical Porous Lithium-Rich Layered Oxide with (110)-Oriented Crystal Planes as a High Energy Density Cathode for Lithium Ion Batteries. *J. Mater. Chem. A Mater.* **2019**, *7* (21), 13120−13129.

(122) Li, F.; Liu, Z.; Shen, J.; Xu, X.; Zeng, L.; Li, Y.; Zhang, D.; Zuo, S.; Liu, J. Ni-Rich Layered Oxide with Preferred Orientation (110) Plane as a Stable Cathode Material for High-Energy Lithium-Ion Batteries. *Nanomaterials* **2020**, *10* (12), 2495.

(123) Jones, W. L.; Kieselbach, R. Units of Measurement in Gas Chromatography. *Anal. Chem.* **1958**, *30* (10), 1590−1592.